New Structure Types among Copper Chalcogenides by Mixing Tellurium with Sulfur or Selenium

by

Mayasree Oottil

A thesis

presented to the University of Waterloo

in fulfillment of the

thesis requirement for the degree of

Master of Science

in

Chemistry

Waterloo, Ontario, Canada, 2010

Declaration

I hereby declare that I am the sole author of this thesis. This is a true copy of the thesis, including any required final revisions, as accepted by my examiners.

I understand that my thesis may be made electronically available to the public.

Mayasree Oottil

Abstract

There is evidence for the existence of non-classical bonding in several binary antimonides, selenides, and tellurides. Owing to such non-classical bonding, some of these solid materials exhibit exciting semiconducting and thermoelectric properties, which make them attractive from a technological view point. However, lack of efficiency is a serious limitation in most of those thermoelectrics. It is very crucial, hence, to find new materials with superior properties and understand the structure and bonding in such materials, in order to facilitate the fine-tuning of the physical properties. With this expectation, several quaternary barium copper chalcogenides are synthesized and characterized in the present study. The chalcogen elements, selenium tellurium, are used in various ratios, in order to understand and tune the binding interactions. Extensive single crystal x-ray diffraction studies are expected to reveal the minute details of the bonding interactions together with electronic structure calculation and physical property measurements. In addition, characterization techniques such as powder x-ray diffraction, electron microscopy, differential scanning calorimetry, thermopower and conductivity measurements are utilized.

The ternary and quaternary chalcogenides, $Ba_2Cu_{4-x}Se_yTe_{5-y}$ were synthesized from the elements in stoichiometric ratios at 700°C, followed by annealing at 600°C. The ternary telluride $Ba_2Cu_{4-x}Te_5$ crystallizes in a new structure type, space group $C2/c$, with lattice dimensions of a = 9.4428(6) Å, b = 9.3289(6) Å, c = 13.3028(8) Å, β = 101.635(1)°, V = 1147.8(1) Å^3, for x = 0.75(1) (Z = 4). The corresponding selenide-telluride adopts another new, but strongly related, structure type, space group $P4_12_12$, with a = 6.5418(3) Å, c = 25.782(2) Å, V = 1103.3(1) Å^3, for $Ba_2Cu_{3.26(2)}Se_{0.729(8)}Te_{4.271}$ (Z = 4). Between 0.13 and 1.0 Te per formula unit can be replaced with Se, while the Cu content appears to vary only within $0.67 \leq x \leq 0.81$ for Ba_2Cu_{4-}

${}_xSe_yTe_{5-y}$. Despite crystallizing in different crystal systems, the telluride and the selenide-telluride exhibit topologically equivalent structure motifs, namely chains of $Cu(Se,Te)_4$ tetrahedra with a Cu atom cis/trans chain as well as an almost linear Te atom chain. All these chalcogenides - as far as measured - are *p*-doped semiconductors, as determined by Seebeck coefficient and electrical conductivity measurements.

Two new orthorhombic chalcogenides, $Ba_2Cu_{6-x}Se_yTe_{5-y}$ and $Ba_2Cu_{6-x}S_yTe_{5-y}$ were synthesized at 800°C. They are isostructural and crystallize in a new structure type, with space group *Pbam*. $Ba_2Cu_{6-x}STe_4$, with a = 9.6560(6) Å, b = 14.0533(9) Å, c = 4.3524(3) Å and $Ba_2Cu_{5.64}Se_{1.09}Te_{3.91}$ with a = 9.7048(6) Å, b = 14.1853(9) Å, c = 4.3840(3) Å. They have Cu_6 units extending along *c*-axis, and two such units are interconnected by S or Se atoms along *a*-axis. These compounds are nonmetallic with low Seebeck coefficients.

Two more new quaternary chalcogenides were uncovered, $BaCu_{5.926(15)}SeTe_6$ and $BaCu_{5.72(16)}Se_{0.464(15)}Te_{6.536}$ with a = 6.9680(2) Å and a = 6.9888(4) Å, respectively, in space group $Pm\bar{3}$. These compounds have basic Cu_8Te_{12} frameworks, which can be an important feature for thermoelectric materials. Ba occupies the void. One Cu atom from each cage cluster of eight such cages forms a Cu_8 cube with Se atom occupying it. $BaCu_{5.9}SeTe_6$ was experimentally determined to be *p*-type doped semiconductor with moderate Seebeck coefficient value.

Acknowledgements

I express my whole-hearted gratitude to my research supervisor, Prof. Holger Kleinke for his excellent guidance, encouragement and enormous support during my studies at Waterloo. He is a great source of inspiration for me and I thank him for directing me to the wonderful area of solid state chemistry.

Many thanks to Dr. Assoud, our crystallographer for his valuable advices and help. I also want to thank Katja, our research associate for all her helps and support. I am extremely grateful for all my colleagues in Kleinke's lab, Abdul, Annie, Bryan, Chris, Dong, Katja, Mariya, Michael, Raj, Savi, Suzan, Tingting and Yanjie for creating a wonderful working atmosphere and for their friendship.

I am also thankful for my committee members: Prof. R. T. Oakley and Prof. S. Lee for their helpful comments and suggestions.

I thank my parents and family members for their love and support throughout my life. I express my special thanks to my husband for his advice, support and love at all difficult times.

Mayasree Oottil

Table of Contents

List of Figures

List of Tables

...until you synthesize that molecule, no one can study its properties. The synthetic chemist is quite in control.

-Roald Hoffmann (*Angew. Chem., Int. Ed. Engl.*, **1987**, *26*, 846)

Chapter1 Introduction

Inorganic molecules and solids exhibit a wide range of chemical and physical properties that have become extremely important in the advancement of science and technology. Understanding the nature of bonding and structure of molecules and solids is of utmost importance not only to explain their various physical properties but also to exploit those properties for various technological applications by means of carefully tuning the binding interactions between the constituent atoms.

1.1 Thermoelectric effect

Thermoelectric phenomenon is mainly referred to two main effects such as Seebeck effect and Peltier effect. It was found that application of a thermal gradient at a bimetallic junction caused an electric potential difference and hence a current flow in the circuit. This thermoelectric effect is called Seebeck effect. The inverse effect, called the Peltier effect, is that a temperature difference would be produced upon applying a voltage across a bimetallic junction. The Seebeck effect offers the possibility of using this phenomenon in the generation of electricity [1]. So an important application of the thermoelectric materials could be converting the waste heat, generated from different sources like automotive exhaust, home heating and industrial processes, to electricity [2, 3]. A good thermoelectric material should possess a high Seebeck coefficient and low thermal conductivity in order to maintain the temperature gradient at the junction [1] (figure 1.1). The potential of a material for thermoelectric application is determined largely by the materials 'Figure of merit',

$$ZT = \frac{S^2 \sigma T}{\kappa} \quad (1.1)$$

Where S, σ and κ are the Seebeck coefficient (also called thermopower), electrical conductivity and thermal conductivity, respectively. The total thermal conductivity consists of two contributions, *i.e.*, from lattice and electrons $\kappa_{tot} = \kappa_{el} + \kappa_{ph}$. A good thermoelectric material should have low thermal conductivity contribution from the phonon part since the electronic component κ_{el} is proportional to electrical conductivity. The factor $S^2\sigma$ in the equation for figure of merit is called the power factor.

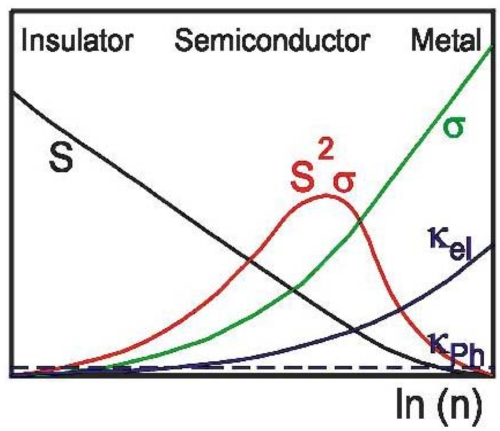

Figure 1.1 Dependence of S, σ, κ, ZT and $S^2\sigma$ on charge carrier concentration.

Generally, metals are poor thermoelectric materials because they have high electrical conductivity (σ) and high thermal conductivity, due to the electronic contributions, κ_{el} but low Seebeck coefficient (S). Insulators are not good thermoelectric materials either: though they have high Seebeck coefficient, their electrical conductivity is very poor. The best thermoelectric materials thus are semiconductors. Some of the important thermoelectric materials such as Bi_2Te_3, PbTe, filled skutterudites-type cobalt antimonides etc. possess ZT values around 1.

1.2 Thermoelectric efficiency and Thermoelectric materials

The dimensionless figure of merit, ZT determines the efficiency of the power generating device, i.e. higher ZT values give better thermoelectric performances. The power generation efficiency is,

$$\eta = \frac{T_H - T_C}{T_H} \frac{\sqrt{1+ZT}-1}{\sqrt{1+ZT}+T_C/T_H} \tag{1.2}$$

T_H and T_C are the temperatures of the hot and cold end respectively.

Though thermoelectric materials are reliable, scalable and environmental friendly devices, they have an important weak point, i.e. their low efficiency. Some well-known thermoelectric materials with their ZT values are shown in the figure 1.2. Efforts are currently being made by various research groups around the globe in order to find highly efficient thermoelectric materials. Therefore, it is extremely important to know the fundamental factors controlling thermoelectric efficiency, which is largely dependent upon the crystal structure and bonding interactions in a particular material.

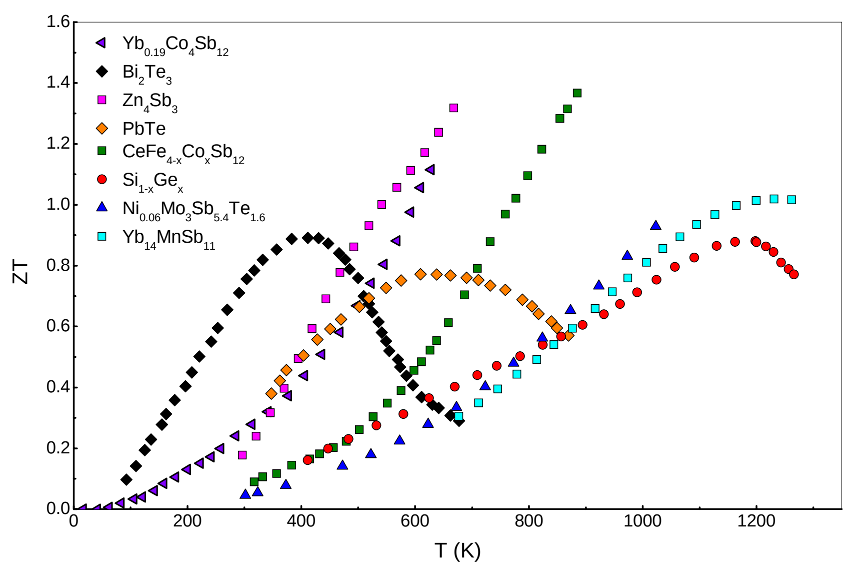

Figure 1.2 Figure of merit, ZT for some thermoelectric materials shown as a function of Temperature.

Generally, semiconductors are superior thermoelectric materials to metals owing to their higher ratio of electrical conductivity to the thermal conductivity, combined with high Seebeck coefficients. A large number of metal chalcogenides exhibit semiconducting behavior and excellent thermoelectric properties. Since the electro-negativities and sizes of S, Se, and Te differ, it is possible to obtain huge variety of interactions between these chalcogen atoms, and hence to obtain semiconductors with different band gaps by conveniently selecting the chalcogenide ions. Also, they generally form complex structures, which typically occur with low thermal conductivity. Due to these reasons, the chalcogenides are considered to be among the best thermoelectric materials. For example, Bi_2Te_3 and its derivatives such as $Bi_{2-x}Sb_xTe_3$ and $Bi_2Te_{3-x}Se_x$, PbTe, $AgSbTe_2$ and its derivatives, are excellent thermoelectric materials [1].

Another class of compounds of interest in thermoelectric research is antimonides. There are various types of unconventional Sb–Sb interactions reported in different compounds. In β-Zn_4Sb_3 [4] and filled skutterudites such as $CeFe_3CoSb_{12}$, [2] Sb–Sb bond distances of typical single bond length and long, slightly bonding interactions are reported. $Yb_{14}MnSb_{11}$, which is considered to be a very good thermoelectric material,[5] contains Sb_3^{7-} units which are isoelectronic with XeF_2 and I_3^- with an overall bond order of ½. In Mo_3Sb_7, which is metallic, Sb_8 cubes are formed, with long Sb–Sb interactions (Figure 1.3). Partial replacement of Sb by Te in this compound, results in semiconducting behavior as observed in $Mo_3Sb_5Te_2$ [6,7]. In all of these compounds, the unconventional bonding interactions play an important role in their conducting and thermoelectric behavior.

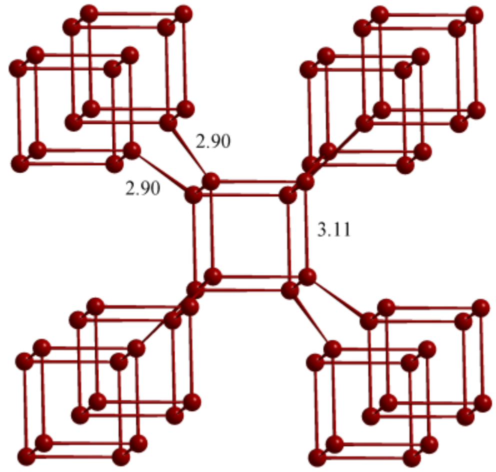

Figure 1.3 Sb substructure in Mo_3Sb_7 [8]

Thus, the band gap, and hence the thermoelectric properties, in such semiconducting materials is essentially controlled by the bonding between the constituent atoms and its structure. Hence it is a primary requirement to understand the structure, basic bonding interactions, and the band structure of the material in order to correlate and thus improve its properties. In the succeeding part of this chapter, the structure and unconventional interactions of some antimonides, tellurides and selenides are discussed briefly. These compounds are generally semiconductors with a narrow band gap, which is ideal for thermoelectrics.

The bonding principles in molecules can be extended to appreciate the bonding characteristics in such solids. For example, to explain bonding in Sb_3^{7-} ion in $Ca_{14}AlSb_{11}$, formation of Sb–Sb half bonds is suggested which are longer than Sb–Sb single bonds (2.80–2.85 Å). Experiments show a Sb–Sb distance of 3.20 Å in the above mentioned linear Sb_3^{7-} unit [9,10]. Such unconventional bonding interactions are often encountered in many solids that contain anions of lower *p*-block elements as in some Zintl phases, pnictides and polychalcogenides. These solids generally contain ionic and covalent types of bonding, which results in interesting physical properties.

Zintl phases form a class of compounds, which is electronically positioned between intermetallics and insulators [11]. A Zintl phase, AQ_n, is the product of the reaction between the late main group elements *Q* (groups 13–16) and alkali metals and alkaline earth metals, A. According to the Zintl-Klemm concept, the valence electrons are transferred from the less electronegative atom, A, to the more electronegative atom, *Q*, which in turn achieves its octet by forming homonuclear *Q*–*Q* bonds. A classical example is NaTl, in which Na gives away its valence electron to Tl, to form Tl^-, and according to the 8-N rule [N= sum of formal charge and main group number], 8- 4 = 4, Tl^- requires 4 more electrons to achieve an octet. This is realized by forming 4 Tl–Tl single bonds per Tl. A diamond-like network of Tl atoms is the result. Another example is Sb in Zintl phases, ASb_x. Sb forms various types of substructures in ASb_x. According to the 8-N rule, a neutral Sb atom can form 3 bonds, Sb^- in KSb can form 2 bonds, whereas Sb^{2-} in $(Na^+)_2(Sr^{2+})_3(Sb^{2-})_4$ can form only one bond [9]. Some of these Sb substructures are shown in figure 1.4.

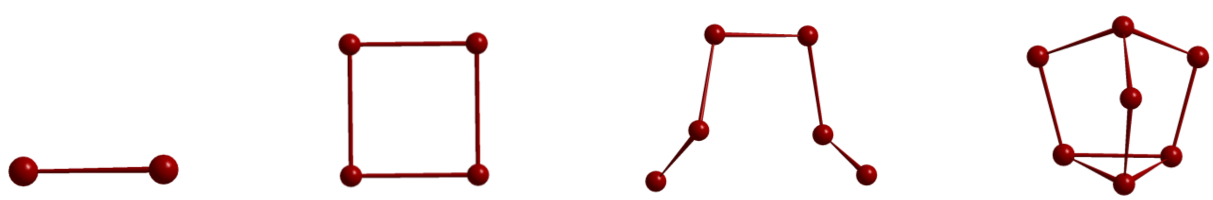

Sb_2^{4-} in $Na_2Sr_3Sb_4$ Sb_4^{4-} in $CoSb_3$ Sb_6^{4-} in Sr_2Sb_3 Sb_7^{3-} in Cs_3Sb_7

Figure 1.4 Selected Sb atom substructures in Zintl phases[12-14].

However, the Sb atom substructure in K_5Sb_4 cannot be explained by the Zintl concept. The Sb_4 unit in this compound is found to be a flat zig-zag tetramer. This would require Sb_4^{6-} fragments to be formed, if all the bonds were classical single bonds, which actually is not the case. The observed bond lengths of 2.79 and 2.81 Å are possibly shorter than typical Sb–Sb single bonds (2.80–2.85 Å). This is explainable by the partial π bonding character and is supported by *ab initio* calculations as well as experimental studies [9].

Many polychalcogenides show unconventional bonding with bond distances and bond angles that are different from those of conventional bonding, namely the oligomeric anionic chains X_n^{2-} [n >2, X = S, Se, Te]. The history of telluride anions dates back to 1900, when Hugot studied the reaction of sodium with tellurium in liquid ammonia. A few years later, stoichiometries of Te^{2-} and Te_4^{2-} anions were deduced by Kraus. Later Te_2^{2-} anions were also identified by Zintl *et al* [15]. In 1970s, scientists' interests were on transition metal chalcogenides due to their special physical properties. The Te–Te bonds in many of these compounds were found to be longer than the ideal Te–Te single bond (2.80 Å). Also, deviations from classical Te–Te bonding was observed in main group tellurides such as TlTe and Ga_2Te_5, in which the Te–Te distances are found to be 3.05 Å and 3.03 Å respectively [16].

In late 1980s, the structural chemistry of tellurium-rich tellurides were reported to behave different to that of chalcogen-rich selenides and sulfides, which were found in helical zig-zag chains X_n^{2-} [n = 4, 5.., Q = S and Se]. The tellurium-rich tellurides showed a variety of structural possibilities, with different anionic fragments. The size of such fragments depends on the formal charge of Te, with the most electron rich anionic component remaining as small, isolated, quasimolecular fragments. On the other hand, some other tellurides show infinite, 1, 2 or 3-dimensional networks of tellurium based on Zintl-Klemm concept [17].

In simple binary alkali metal pentatellurides M_2Te_5, [M = Rb, Cs], had the Te–Te distances of 3.05 Å been ignored (i.e. no bonding interactions), the compound would be made of Te^{2+} cations, 2 Te^{2-} anions and 2 M^+. It is logical to consider the Te–Te distances of 3.05 Å as (half) bonding interactions. Then it will be $M_2Te_5 = 2M^+ + {}^1_\infty[Te_5^{2-}]$ (Figure 1.5). So the resulting structure resembles the square planar XeF_4 structure.

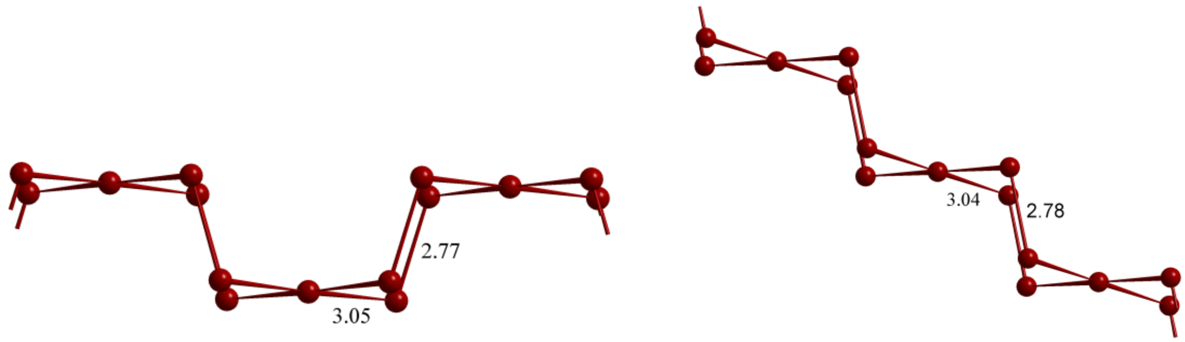

Figure 1.5 Polyanionic structure of M_2Te_5 [M = Rb, Cs][18,19] .

Square planar XeF_4 has 36 valence electrons, whereas Te_5^{2-} has only 32 electrons, and one would expect the latter to be tetrahedral. But, Te_5^{2-} is square planar, and this is stabilized by interconnecting these fragments by the terminal tellurium atoms to compensate its lack of electrons [20]. This 32-electron fragment can also be stabilized by the addition of two single tellurium atoms as in Re_2Te_5 (Figure 1.6 a), or by the addition of two Q_3 groups to form anions of the type $TeSe_{10}^{2-}$, Se_{11}^{2-} etc, [16] as shown in Figure 1.6 b.

The Te_5^{6-} anion, which is isoelectronic with XeF_4, also exists in M_2SnTe_5 (M = K, Rb, Tl) or Ga_2Te_5, which comprise of electron rich 3 center bonds with Te–Te distances of greater than 3.00 Å. Another closely related entity is Te_8^{8-} as found in Tl_2GeTe_5. It should be noted that a square ring of Te atoms is formed here, with Te–Te distances of 2.92 Å and 3.12 Å at the central square and at the terminals respectively (Figure 1.6 c). In In_2Te_5, Te forms one dimensional infinite chain with Te–Te distances of 2.86 Å and 3.36 Å suggesting different bonding interactions (Figure 1.6 d). Similarly, the infinite Te chain in TlTe as shown in Figure 1.6 e, has Te–Te distances of 3.02 Å and 3.09 Å which indicate weaker Te–Te interactions than in a regular Te–Te single bond.

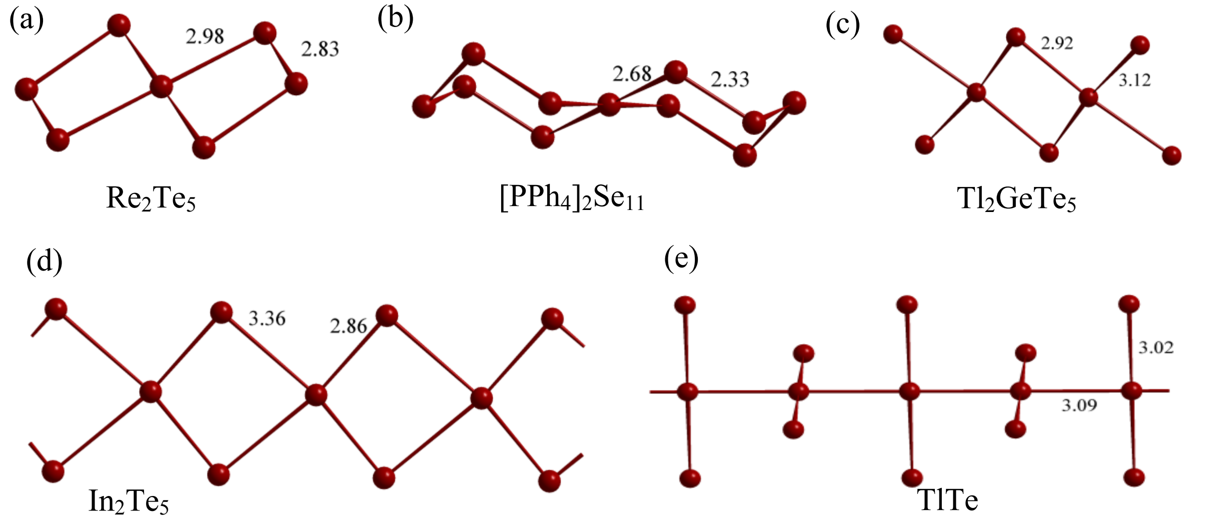

Figure 1.6 Various Te_5^{n-} anions.[16,21-24]

In NaTe and Ba_2SnTe_5, 34-electron Te_5^{4-} anions are found as $6NaTe = 6Na^{+} + Te_5^{4-} + Te^{2-}$ and $3Ba_2SnTe_5 = 6\ Ba^{2+} + [Sn_3Te_{10}]^{8-} + Te_5^{4-}$. They can be described as 2 Te atoms added to a Te_3^{4-} linear fragment to compensate its electron deficiency (Figure 1.7a). The central linear fragment with Te–Te bonds of 3.02 and 3.10 Å shows half-bonding interactions (with 3c–4e bonding) and the other two terminal Te atoms in the trans positions form shorter Te–Te single bonds (2.82 Å)[25].

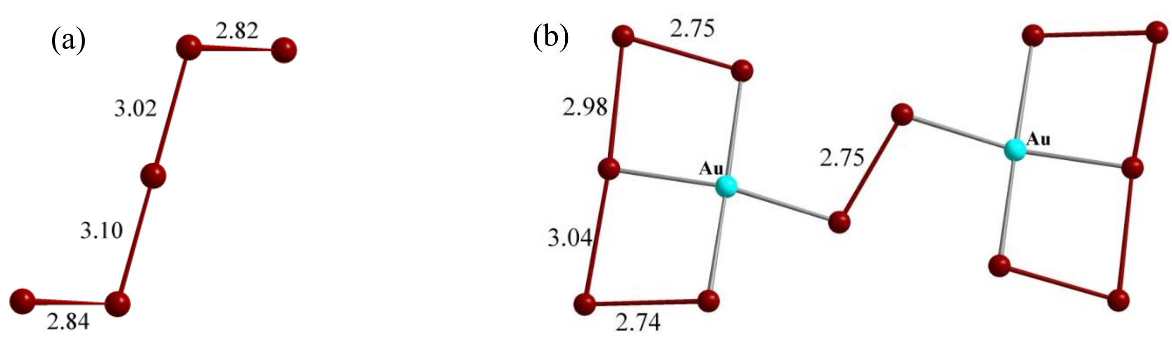

Figure 1.7 a) The bent Te_5^{4-} anion[25] (trans) and (b) $[Au_2Te_{12}]^{4-}$ anions[16] (cis).

The anionic fragments, Te_5^{4-} can be stabilized by adding transition metals. An example is stabilization of the Te_5^{4-} anion by Au atoms. This results in the anions with terminal Te atoms in cis position to each other (or U-shaped)[16] in $[Au_2Te_{12}]^{4-}$. In this case, the Te_5^{4-} anion is considered as an η^3-ligand,[25,26] Figure 1.7b.

Another interesting entity is the two-dimensional infinite layer of 18 membered tellurium rings as observed in $CsTe_4$. This consists of 25-electron Te_4^-, which forms bonds with other Te_4^- fragments to compensate the lack of electrons (Figure 1.8). It is interesting to note that Te–Te distances vary from 2.75 Å to 3.14 Å suggesting in part fractional bond orders. The structure of $CsTeSe_3$ can also be explained in the same manner, which suggests Se also could exhibit unconventional bonding to form such two-dimensional layers.[16]

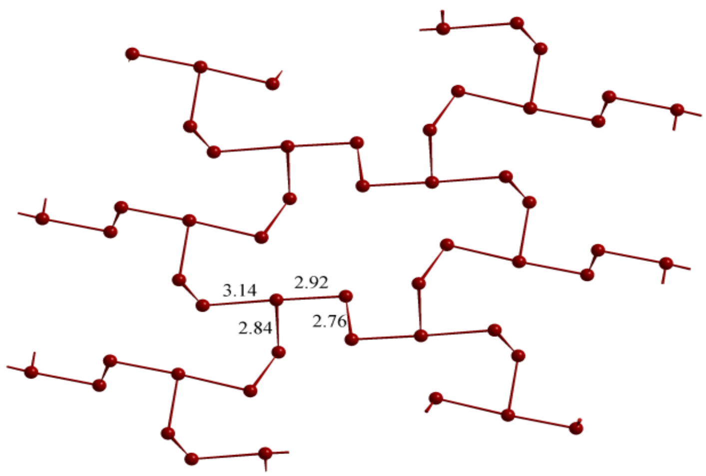

Figure 1.8 Structure of Te_4^- entity in $CsTe_4$.[27]

Non-classical bonding is observed in materials having planar square nets of main group elements, as $NdTe_3$ with square nets of Te. Distorted square nets were also observed in some cases like $LaSe_2$, $LaTe_2$, Cs_2Te_2 and $K_{0.33}Ba_{0.67}AgTe_2$ [16](Figure 1.9).

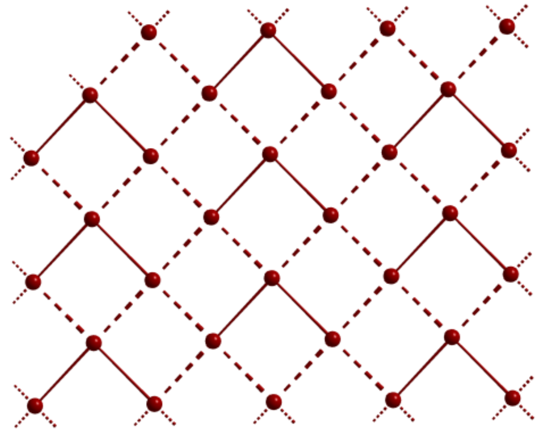

Figure 1.9 Distorted square nets of Te in $K_{0.33}Ba_{0.67}AgTe_2$.[26]

It was found that in some cases selenium also behaves similar to tellurium. An example is the presence of linear Se_3^{4-} with 3c–4e bonding in $Ba_2Cu_xAg_{4-x}Se_5$, which exhibits semiconducting properties.[28] In all the above cases unconventional bonding of Te or Se was found. In most cases Te–Te distances are found to be longer than the single bond distance of 2.80 Å. Many salts of chalcogenides (Se, Te) exhibit semiconducting properties. Many of them show a significant thermoelectric effect and have been in the limelight of thermoelectric research for several decades.

Chapter 2 Motivation and Outline

2.1 Background Research

Following the encouraging reports about the thermoelectric properties[29-31] of $BaCu_2Te_2$[32] and $A_2BaCu_8Te_{10}$ (A = K, Rb, Cs),[33] we began to systematically investigate the Ba/(Cu,Ag)/(Se,Te) system. Thereby, several new polychalcogenides were discovered, namely first $Ba_3Cu_{14-x}Te_{12}$ with Te_2^{2-} dumbbells, and very low thermal conductivity,[34] then second $Ba_{6.76}Cu_{2.42}Te_{14}$ with bent Te_3^{2-} units,[35] followed by $Ba_2Ag_4Se_5$ and its Cu-substituted variants with the first linear Se_3^{4-} unit ever found[28] and $Ba_3Cu_{17-x}Se_{11-y}Te_y$ with independent Q^{2-} atoms.

The compound $Ba_7Au_2Te_{14}$ and its Cu variant, which are of $NaBa_6Cu_3Te_{14}$ [36]structure type in hexagonal $P6_3/mcm$ space group has characteristic V-shaped Te_3^{2-} units. Its copper variant has a different stoichiometry from that of ternary gold-telluride, i.e. $Ba_{6.76}Cu_{2.42}Te_{14}$, where an additional site is occupied by Cu which is deficient. The following figure 2.1 a shows these V-shaped Te_3 units.

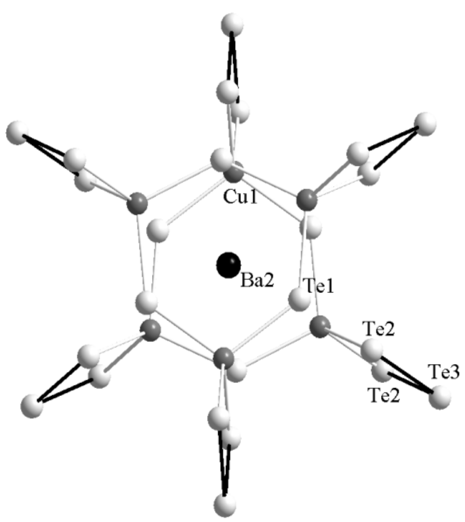

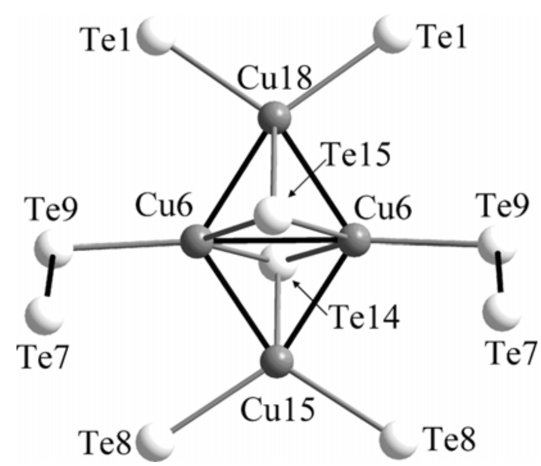

Figure 2.1 (a) Te_3 units attached to Cu_3Te_3 rings in $Ba_{6.76}Cu_{2.42}Te_{14}$,[35] (b) $CuTe_3^-$ units with Te_2^{2-} dumbbells in $Ba_3Cu_{14-x}Te_{12}$.[34]

Cu deficiency is also observed in $Ba_3Cu_{14-x}Te_{12}$ (space group: $P2_1/m$). This structure consists of edge, corner and face-sharing $CuTe_4$ tetrahedral units connected with unusual, almost planar $CuTe_3$ units, figure 2.1 b.

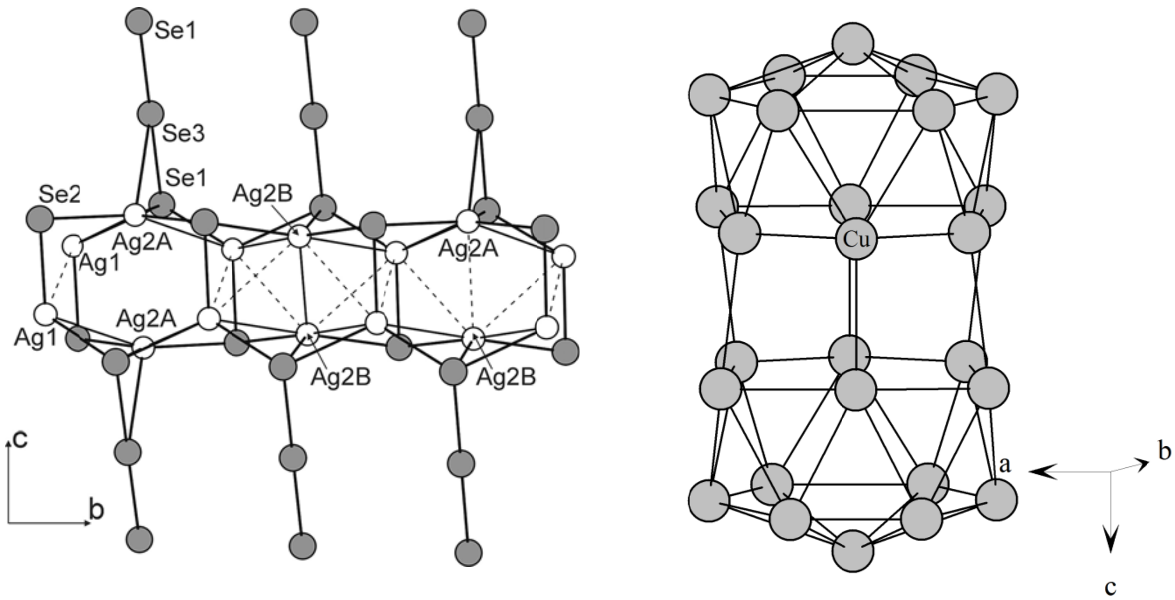

Figure 2.2 (a) Linear Se_3^{4-} units in $Ba_2Cu_\delta Ag_{4-\delta}Se_5$[28] (b) Cu_{26} clusters of $Ba_3Cu_{17-x}Se_{11-y}Te_y$[37]

$Ba_2Ag_4Se_5$ and its Cu-substituted variant were the next interesting new structures that we discovered in our research group. These compounds consist of unique linear Se_3^{4-} units, figure 2.2 a.

Using both selenium and tellurium within one reaction, we succeeded in uncovering another new structure type, adopted by $Ba_3Cu_{17-x}Se_{11-y}Te_y$[37], which neither exists as a pure selenide nor as a pure telluride. This compound, which consists of Cu_{26} clusters with proven Cu ion mobility was another interesting one in Ba-Cu-*Q* system published in early 2009 (figure 2.2 b.).

The compounds containing Ba– Cu/Ag– *Q*'s that were discovered are shown in one simple ternary phase diagram in the following figure 2.3 (including the ones which are described/

reported in the following chapters). In this phase diagram the quaternary compounds are considered as ternaries by representing the different chalcogenides as *Q*.

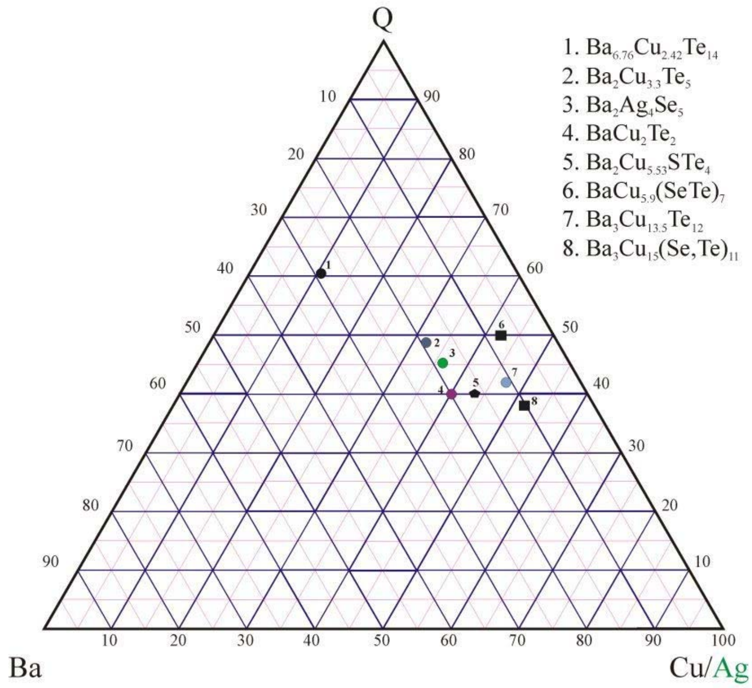

Figure 2.3 Ba-Cu/Ag-Q phase diagram

Thus, the present study is based on the bonding in Se, Te quaternaries, their crystal structure studies as well as thermoelectric properties. Attempts were made to utilize such unconventional bonding to form complex structured semiconductors, which might exhibit improved thermoelectric properties. Quaternary variants of Ba–Cu–Te compounds, with substitution at Te-site by Se are studied. The research plan was to synthesize quaternary selenide– tellurides with Ba and Cu as cations in pure form, to solve their structure using single crystal and powder x-ray diffraction methods, to calculate the electronic structure using Linear Muffin–Tin Orbital (LMTO) method, (thus to study the Se–Se, Se–Te, Te–Te interactions and the Se, Te ordering in this compound), and finally, to measure the thermoelectric power, electrical conductivity and thermal conductivity properties. Based on these studies, the bonding-structure-property relationships in these compounds are explained.

2.2 Experimental methods

2.2.1 Synthesis

Barium copper chalcogenide samples are prepared from the individual, pure elements. (Ba: Aldrich, 99%; Cu: Alfa Aesar, 99.9%; Te: Alfa Aesar, 99.99%; S: Alfa Aesar, 99.999%; and Se: Aldrich 99.99%). These elements are weighed in the required stoichiometry inside an Argon-filled glove box. The elements are weighed into quartz tubes, which are then closed using vacuum-tight valves, taken out of the glove box and evacuated immediately till the pressure reaches around 1–3 x 10^{-3} mbar. The quartz tubes are then sealed using a hydrogen-oxygen torch. The sealed ampoules are then placed in programmable furnaces. The heating profile is selected depending on the nature, amount and ratio of the reactants. After annealing the samples for sufficiently long duration, they are either slow-cooled or quenched into water. The samples are ground using an agate mortar and pestle and are either subjected to further annealing or used for further analyses.

2.2.2 Direct (ceramic) method

The most widely used method for preparing solid materials is direct reaction of solid components at high temperature. It is necessary to have high temperature in order to have a proper reaction rate. Solids usually do not react with each other at room temperature even if the products are thermodynamically favored. Despite the fact that high temperatures are needed to initiate the reaction, both thermodynamic and kinetic factors are important.

2.3. Sample analyses

2.3.1. Powder X-ray diffraction

Powder X-ray diffraction technique is mainly used for

i) Phase purity analysis, and

ii) To study the crystal structure.

An INEL X-ray diffractometer is used during the present research work (figure 2.5). X-rays are generated by the bombardment of electrons on a target such as Cu. Thus emitted rays consist of a range of wavelength with varying intensities, thereby giving an X-ray spectrum of the target. In order to get a monochromatic beam of X-rays emitted from Cu, Nickel filters or monochromaters are used. A crystal with its regularly repeating unit cells or atomic layers can be viewed as an optical grating. The crystal should then, diffract radiation that has a wavelength similar to the interatomic separation (approximately 1Å). Diffraction of crystals can be demonstrated as shown in Figure 2.4.

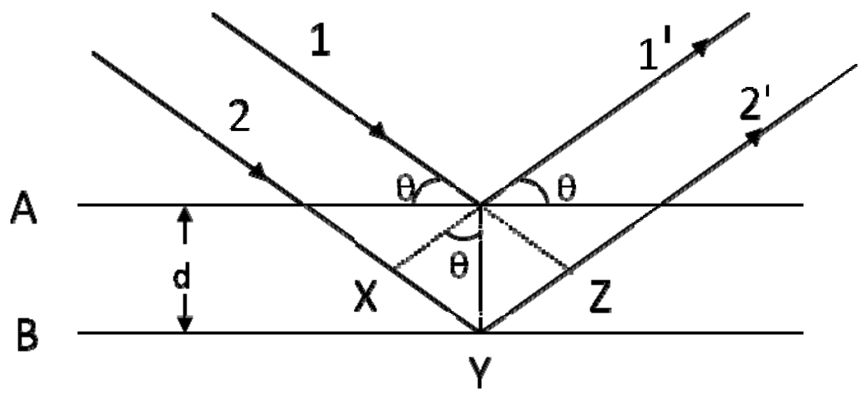

Figure 2.4 Diffraction of X-rays from a crystal – Bragg's law

A and B are two adjacent planes in a crystal separated by a distance d. X-ray beams 1 and 2 are reflected from these planes along 1'and 2' which are *in phase* if the path difference XYZ is equal to whole number multiple of wavelength of X-ray used. Thus,

XY = YZ = d sinθ, where θ is the angle of incidence.

XYZ= 2d sinθ

If 1' and 2' are in phase, XYZ= $n\lambda = 2d \sin\theta$, this is known as Bragg's law.

This results in the constructive interference of reflected rays. At all angles except Bragg's angle, the reflected beams are *out of phase* and consequently, they interfere destructively.

During the process of X-ray diffraction by crystals, it is actually the atoms or ions that act as secondary point sources and scatter the X-rays, since the X-rays interact with the oscillating electric field of an atom (or electrons around the atoms) in a crystal. This essentially makes each electron of an atom to vibrate and this results in emission of radiation which is *in phase* (or coherent) with the incident beam. The efficiency of scattering of a particular atom is called as the scattering factor, commonly denoted as f.

$$f = \frac{\text{Amplitude of wave scattered by an atom}}{\text{Amplitude of wave scatterd by an electron}} \qquad (2.1)$$

A crystal often is made up of several types of atoms. The resultant wave scattered by all the atoms in a unit cell is generally known as structure factor F, which is obtained by summation of the scattering factor contribution from individual atoms. For a unit cell of n atoms, (n = 1,2,3..) with fractional coordinates (x_u, y_u, z_u) and scattering factors f_1,f_2,f_3..f_n, the structure factor can be expressed as,

$$F\ (hkl) = \Sigma\ f_j \exp\ [2\pi i\ (hx_j + ky_j + lz_j)] \qquad (2.2)$$

(a) (b)

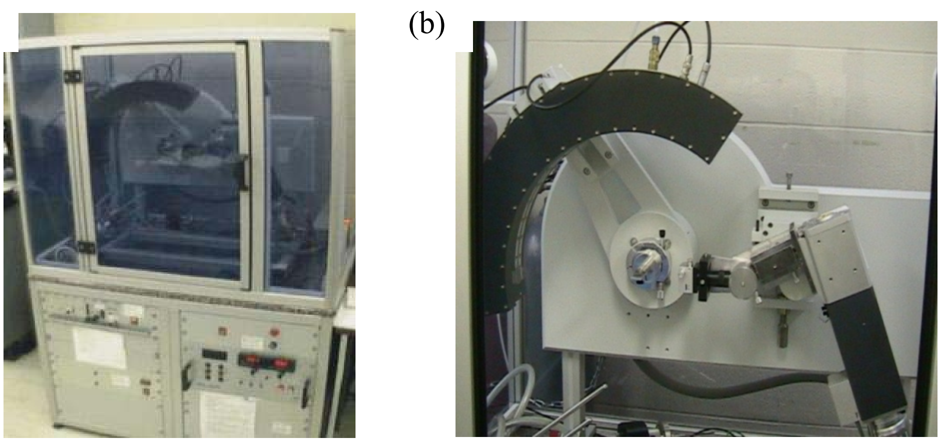

Figure 2.5 (a) Powder Diffractometer (b) Detector.

The experimental powder diffraction patterns thus obtained may be indexed and refined using various computer programs.

2.3.2. Single crystal XRD analysis

Single crystal X-ray diffraction method is used to solve the crystal structures. The analysis includes determination of unit cell dimensions, bond lengths, bond angles, details of site ordering and finally yields the complete crystal structure.

The first step of this method would be to choose an appropriate single crystal. Usually, the dimensions of the crystal should be less than 0.5 mm and the minimum thickness should be 0.01 mm. The crystals can then be mounted on a glass fibre for the data collection.

The theory of this method is based on Bragg's law as discussed earlier. Here molybdenum is used as the target material and the wavelength of Mo K_α radiation is 0.7107Å. These X-rays are first collimated and then directed onto the crystal. The diffraction phenomenon occurs only when Bragg's condition is satisfied. These rays are detected by a charge coupled device (CCD) detector (which transform the X-ray photons to the electrical signals). The data collection and processing are generally done by a computer. A Bruker single crystal diffractometer (Figure 2.6) is used for the single crystal studies. Apex CCD detector is used to detect the diffracted X-rays and these signals are sent to the computer. "SMART" software is used for the data collection and unit cell determination (at the Department of Chemistry in University of Waterloo). The data reduction is the next step, where the raw data are corrected for Lorentz and Polarisation effects and this is done by 'SAINT'[38] programme. The space group determination is done by using XPREP embedded in the SHELXTL[39] package. The SHELXTL package, in general, is used for the absorption correction, structure solutions and refinement. The quality of the solution is assessed by the parameters, R1, wR2 and GOOF. R1 displays the agreement between the calculated and the observed models. Ideally it should be zero, which is seldom obtained. In most cases, it should be less than 5%. R1 is given by, R1= $\Sigma| |F_o| - |F_c| | / |F_o|$

wR2 is called the weighted R factor, and it is usually greater than R1, because it is based on F^2. wR2 should be less than 10% for a decently refined structure. GOOF is the goodness of fit, which should approach 1, for a good refinement.

Figure 2.6 Single Crystal Diffractometer

2.3.3. Energy dispersive X-ray analysis

Energy dispersive X-ray analysis is a technique used for characterization of elements in a sample and its stoichiometry. This technique is often applied in conjunction with Scanning Electron Microscope.

When a beam of charged particles with sufficiently high energy, such as electrons, hits the sample surface, the core electrons of the atoms within the sample are knocked off. Consequently, electrons from the outer shell then fill the hole created by the ejection of the core electron, and an energy equal to the difference between the higher and the lower energy levels is emitted in the form of X-rays. This is measured in the form of an energy dispersive spectrum. The X-rays thus emitted will be characteristic of a particular atom. Thus different elements will have different peaks in the spectrum, which can be used as finger prints. The integration of the area under the curve/peak of each element directly gives the relative quantities of each element in the sample. This enables one to identify the type of atoms or the stoichiometry of the sample, although there are various factors which form hurdles to assess accurate stoichiometry of a compound. EDX is a versatile technique when used with other complimentary techniques such as XRD. The EDX analysis is performed by using LEO 1530 FESEM integrated with EDX Pegasus1200 (Figure 2.7 a) in the Department of Chemistry at the University of Waterloo.

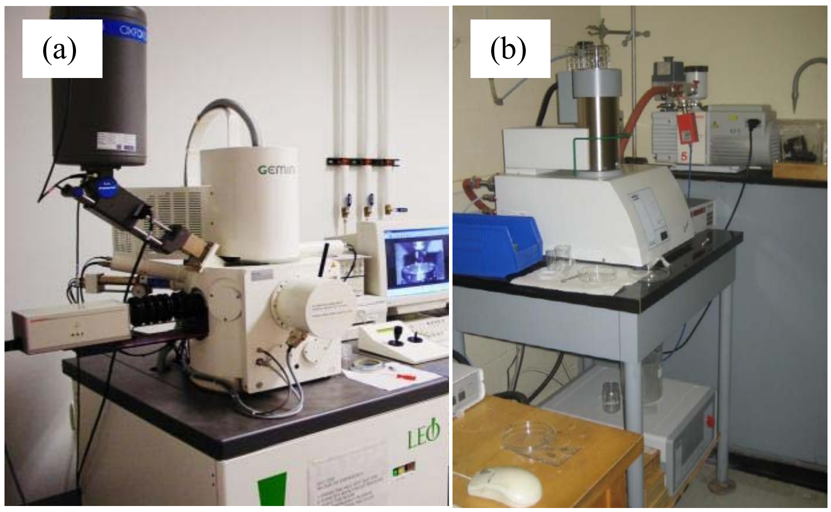

Figure 2.7 (a) SEM with EDX (b) DSC with TG

2.3.4. Thermal analysis

Thermal analysis is often used to study the thermal stability and decomposition, fusion and other phase changes. In the present study, two thermal analysis methods are employed; thermogravimetry (TG) and differential scanning calorimetry (DSC). In TG, a change in the weight of substance is recorded as a function of temperature. This helps in a way to understand the thermal decompositions (if at least one of the decomposed phases is in gaseous state). DSC is employed mainly to evaluate the melting point of the sample and /or any phase transitions. This technique is based on measuring the differential energy that is required to keep both the sample and reference material at the same temperature. Thus, this study allows to detect endothermic or exothermic processes while the temperature of the sample is changed.

Knowledge of melting point of the sample is important, since, this would help to divide the heating profile to synthesize the sample and to grow large enough single crystals for various other measurements.

A NETZSCH STA 409PC Luxx instrument is used for such studies (figure 2.7b). An operating temperature range of 30-1600°C is possible, and the measurements are carried out strictly under Argon gas atmosphere.

2.3.5. Electronic structure calculation (L.M.T.O)

The electronic properties of solids, such as electronic conductivity and Seebeck effect, are closely related to the structure and bonding in solids. Electronic structure calculations, thus become extremely important for predicting, verifying and understanding the physical properties in solids. Important concepts that need special mention in this context are band dispersion (tight binding approximation: bands are formed by linear combination of atomic orbitals) and Density of States or DOS (number of energy levels between a small energy element). The band dispersion curves directly give the band gap of the material, if present, which in turn help predicting or verifying the semiconducting, metallic or insulating behavior of the material, depending on the position of Fermi energy or Fermi level (which is the highest occupied energy level). Also, since the carrier mobility is directly proportional to the slope of the band (Fermi level), large band dispersion or band width may be expected to result in increased carrier mobility and hence increased electrical conductivity. DOS and partial DOS (contribution from individual elements to the total DOS) provide information about which orbitals contribute in a specified energy range. This is particularly important when partial substitution and ordering might affect the electronic properties. Also, it is shown that Seebeck coefficient (S) of a material is proportional to the first derivative of the DOS with respect to energy above and below the Fermi level.

$$S \propto \frac{1}{DOS(E)} \cdot \frac{dDOS(E)}{dE}\bigg|_{E=E_F} \qquad (2.3)$$

Besides these important information, electronic structure calculation gives an idea about the bonding characteristics via the calculation of crystal orbital Hamilton population (COHP),[40] which would directly point out the strength of various interactions existing in solids. This is particularly important in structures consisting of weak interactions such as hypervalent bonds. For the electronic structure calculations reported here, we have used Tight-Binding Linear Muffin-Tin Orbital (TB LMTO) method, developed by Andersen, with the atomic spheres approximation (ASA)[41,42] wherein Muffin-tin spheres are assigned around each atom, with one region being spherically symmetric inside the muffin-tin sphere, and the other is constant outside the sphere. Bloch functions are used in combination with Tight Binding Approximation to yield basis functions. In ASA, it is approximated that, these muffin-tin spheres fill the total volume of the unitcell. Local density approximation (LDA) that employs Density functional theory (DFT) is utilized for the exchange and correlation energies[43]. The electronic calculations mentioned in this thesis were done via LMTO47c program.

2.4 Physical property measurements

2.4.1. Thermal conductivity

Thermal conductivity of the samples is determined by measuring the thermal diffusivity and obtaining the specific heat of the material.Thermal conductivity,

$$\kappa = \alpha\, \rho\, C_p \qquad (2.4)$$

Where α is the thermal diffusivity and ρ is the density and C_p is the molar specific heat. α can be measured using Flash laser method. C_p may be obtained via DSC or the Dulong-Petit limit at elevated temperatures. An experiment setup from ANTER Corporation, viz; Flash line 3000 is used for the determination of κ. Here, the material is subjected to a short laser pulse from the Xenon flash lamp, and by measuring the time required to attain half of the temperature increase, one can calculate α as, $\alpha = 0.1388L^2/\ t_{1/2}$, where L is the length of the sample and $t_{1/2}$ is the time required to reach half of the maximal temperature increase (or half rise time). The experimental setup is shown in the Figure 2.8.

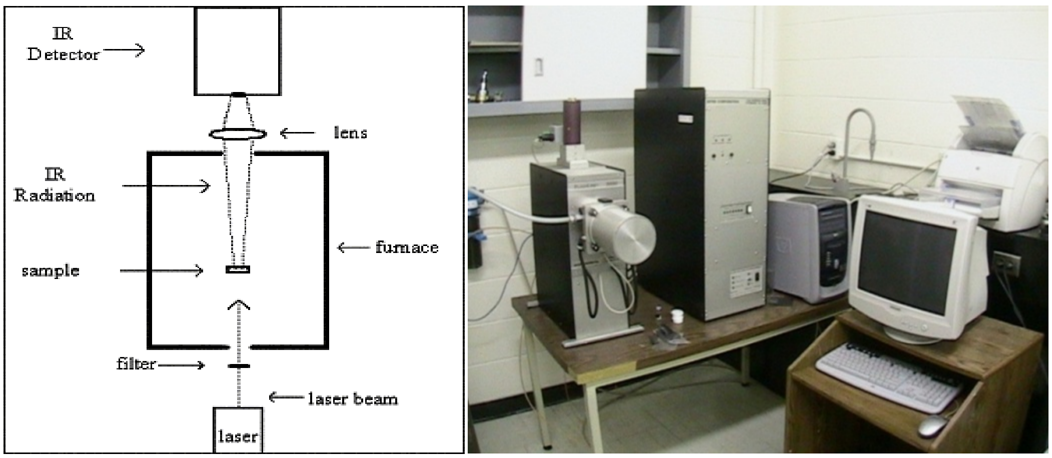

Figure 2.8 Thermal conductivity measurements.

2.4.2. Seebeck and Electrical conductivity measurements

Seebeck coefficient and electrical conductivity measurements were done simultaneously, using ULVAC- RICO ZEM-3 unit. In this measurement, the sample in a rectangular pellet form is kept in an upright position between two electrodes. The pellet size can be varied from 6 mm to 20 mm. Two thermocouple probes are pushed in contact to the sample from the sides, thus making a four point contact for electrical conductivity as well as to measure dT and dV, for Seebeck, as shown in Figure 2.9. Once the sample is placed and covered using a temperature equalizing cap, V-I plot of the sample is measured followed by moving the IR furnace over the sample. The latter is closed, evacuated and filled with helium so that the sample should not get oxidised during the measurement.

For Seebeck measurements, a suitable temperature gradient can be generated by "Delta T" heater, situated at the bottom of the electrode, which is measured using two thermocouples, as $T_1$and T_2. Consequently, potential difference will be produced for the sample, which can be denoted by dV.

$$\text{Seebeck coefficient} = dV/(\text{temp } T_2 - \text{temp } T_1) \tag{2.5}$$

$$\text{Measurement temperature} = (\text{temp } T_1 + \text{temp } T_2)/2 \tag{2.6}$$

A standard four-point probe method is employed for the measurement of resistivity or conductivity. In a typical four wire method, separate pairs of wires are used for providing current through the sample and measuring the voltage across it. Generally, when dealing with the semiconducting samples, four wire method has definitely an edge over the two wire method (the latter may be used when the sample is highly resistive). This is due to the fact that two-wire method does not eliminate the contact resistance and thermal voltage developed at the sample-electrode interface. The four wire method gets around the problem and the measurement provides accurate values of resistivity/ conductivity of the sample.

For the conductivity measurements, resistance, R is calculated from the measured values of current passed through the sample from a constant current supply (I) and Voltage, V between probes T_1 and T_2, using a voltmeter.

$$R=V/I \text{ (Ohm's law)} \tag{2.7}$$

Resistance of a material is proportional to its length, L (distance between the probes T_1andT_2) and area of cross section, A of the pellet,

$$R = \rho L/A; \quad \rho = RA/L; \text{ where, } \rho \text{ is called the resistivity.}$$

$$\text{Conductivity, } \sigma = 1/\rho \ (\Omega^{-1}\text{cm}^{-1})$$

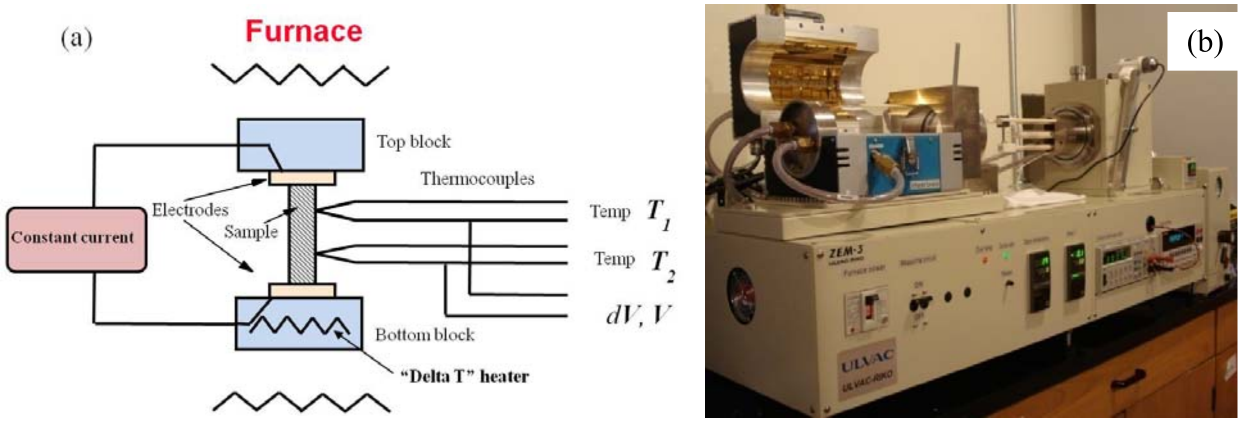

Figure 2.9 (a) Conceptual diagram for ZEM-3 measurement (b) ULVAC- RICO ZEM-3 unit

Chapter 3 Structure change via partial Se/Te substitution: Structure and Properties of the new Selenide-Tellurides $Ba_2Cu_{4-x}(Se,Te)_5$

The Differential Fractional Site Occupancy was originally based on mixing two slightly different metal atoms, such as Nb and Ta, in metal-rich chalcogenides in order to afford a new structure type. The metal atom that is able to form stronger metal-metal bonds tends to prefer the sites with more such bonds. Thereby, most if not all metal sites are mixed occupied with different ratios of the two metal atoms. [44,45] This concept which has proven to be quite successful in the past was employed while designing new sulfides namely $Nb_{1.72}Ta_{3.28}S_2$,[46] $Nb_{0.95}Ta_{1.05}S$,[47] $Nb_{4.92}Ta_{6.08}S_4$[48] and $Nb_{6.74}Ta_{5.26}S_4$.[49] More and more examples were found thereafter, with different metal atoms such as Zr and Ti ($Zr_{4.32}Ti_{2.68}Sb_7$)[50], Zr and V ($Zr_{7.5}V_{5.5}Sb_{10}$)[51], Hf and Nb ($Hf_5Nb_5Ni_3P_5$, [52] $Hf_{1.5}Nb_{1.5}As$[53]), and Ti and Ta ($Ti_{1.3}Ta_{9.7}Ge_8$)[54], to name a few. Subsequently, it became apparent that the same concept may be applied to mixed anionic constituents[55,56]. The compound $Ba_3Cu_{17-x}Se_{11-y}Te_y$, is an example from our research group with applying DFSO concept, which neither exists as a pure selenide nor as a telluride. Examples with Se and Te besides $Ba_3Cu_{17-x}Se_{11-y}Te_y$ are $Ta_{15}Si_2Se_yTe_{10-y}$ [57]and $LnSeTe_2$ with Ln = lanthanoid. With this contribution, we present the first example, in which incorporating Se into a polytelluride changes the structure while retaining the structure motifs.

3.1. Syntheses and Analyses

All elements of purity mentioned in the previous chapter, were used as acquired. The telluride was first found in a (roughly 500 mg) sample starting from Ba, Cu and Te in the 4 : 8 : 13 ratio. The elements were loaded into a silica tube in an argon-filled gloved box, which was then sealed under dynamic vacuum. The fused tube was placed into a resistance furnace, heated to 700°C within 24 hours, and kept at that temperature for four days. Such a temperature was expected to achieve a molten sample. To allow for crystallization, the furnace was slowly cooled to 200°C over a period of 10 days.

After the main product was identified to be $Ba_2Cu_{4-x}Te_5$ (with x = 0.67, space group *C*2/*c*) via a single crystal structure determination described below, we tried to obtain phase pure samples by varying x between 0.5 and 1.0 in steps of 0.1. These mixtures were also heated in fused silica tubes to 700°C for two hours, and then at 600°C for 20 days. To increase homogeneity, the samples were then ground and reheated at 600°C for another ten days. This procedure yielded pure samples for x = 0.7 and 0.8, but not for the others, as determined utilizing the X-ray powder diffractometer (INEL) with position sensitive detector employing Cu-$K\alpha_1$ radiation.

To investigate whether Se atoms may be incorporated into this structure, reactions were carried out with different Se contents, starting from 2 Ba : 3.3 Cu : y Se : (5–y) Te with y = 0.10, 0.25, 0.5, 0.8, 1.0, and 1.5. These reaction mixtures were heated at 570°C for five days, and then slowly (over a period of four days) cooled down to room temperature. Thereafter, the reaction mixtures were ground and then reheated at 550°C for several days. Since all powder diagrams looked distinctly different from the pattern calculated for the $Ba_2Cu_{4-x}Te_5$ model, a single crystal from the sample with y = 0.8 was selected for single crystal structure studies. After the successful structure solution, which resulted in the formula $Ba_2Cu_{3.26}Se_{0.73}Te_{4.27}$ and space group $P4_12_12$, the powder diagrams could be identified as containing exclusively the reflections of this new type for $0.25 \le y \le 1.0$, while the more Se-rich and the more Se-poor sample exhibited additional reflections belonging to minor side products including $BaCu_2(Se,Te)_2$ and BaTe, respectively. One can thus conclude that the Se content of tetragonal $Ba_2Cu_{4-x}Se_yTe_{5-y}$ may vary at least within $0.25 \le y \le 1.0$, but does not reach 0.10 or 1.5.

A differential scanning calorimetry (DSC) experiment carried out under a flow of argon on the sample with y = 0.8, using a NETZSCH STA 409PC Luxx as described earlier, pointed to a melting point of 640°C, and one with $Ba_2Cu_{3.3}Te_5$ to a melting point of 620°C.

The samples of nominal compositions $Ba_2Cu_{3.3}Te_5$, $Ba_2Cu_{3.3}Se_{0.8}Te_{4.2}$ and $Ba_2Cu_{3.3}SeTe_4$ were analyzed via energy dispersive analysis of X-rays using an electron microscope (LEO 1530) with an additional EDX device (EDAX Pegasus 1200). The Ba : Cu : Te ratio, averaged over several crystals, was 20.1 : 31.6 : 48:3 atomic-% for the ternary telluride, which compares nicely with the numbers calculated from the nominal formula (19.4 : 32.0 : 48.6 at-%). In case of $Ba_2Cu_{3.3}Se_{0.8}Te_{4.2}$ (nominal 19.4 : 32.0 : 7.8 : 40.8 at-%), the Ba : Cu : Se : Te ratio was averaged to 18.0 : 34.9 : 9.3 : 37.8 at-%, revealing a significant incorporation of Se.

3.2. Structure determination

A single crystal of the nominal composition "$Ba_4Cu_8Te_{13}$", crystal I, was selected for the structure determination. Data were collected on the Bruker Smart APEX CCD diffractometer with graphite-monochromatized Mo-$K\alpha_1$ radiation, via ω scans of 0.3° in two groups of 606 frames at $\phi = 0°$ and 90°. The crystal was exposed for 60 seconds to the radiation for each frame. The data were corrected for Lorentz and polarization effects. Absorption corrections were based on fitting a function to the empirical transmission surface as sampled by multiple equivalent measurements using SADABS incorporated into the package SAINT.

The SHELXTL program package was utilized for the structure solution and refinements. Based on the lattice parameters, monoclinic *C*-centered was chosen as the Bravais lattice. The systematic absences restricted the possible space groups to *C*2/*c* and *Cc*. Using the "Direct Methods" of SHELXS yielded one Ba, two Cu, and three Te atoms in the space group *C*2/*c*. Subsequent refinements revealed large thermal expansion parameters in case of the two Cu sites, most notably so for Cu1, and significantly anisotropic ones in case of two of the three Te sites, with $U_{22} \approx 2\ U_{11} \approx 2\ U_{33}$. Therefore, the occupancy factors of the Cu sites were refined, yielding deficiencies of 31% (Cu1) and 3% (Cu2), respectively, and split sites were introduced for the Te sites, yielding two additional sites with the smaller occupancies, namely 29% and 33% Te, respectively. Refining the occupancies lowered R1 from 0.082 to 0.067, and introducing the split sites to 0.051 (all data). Studying all measured reflections in reciprocal space, viewed along *a**, *b**, and *c** did not reveal any systematic twinning or an intergrowth crystal. Because no improvements were noticeable in lowering the symmetry to *Cc*, and no evidence for long range ordering via super cell formation was found, the space group *C*2/*c* remained as the final choice. Finally, all atomic positions were standardized with the TIDY program as included in the PLATON package.

To investigate the existence of a phase range and whether or not the Te split sites occur in all cases, two more crystals were analyzed, one from the nominal composition "$Ba_2Cu_{3.3}Te_5$", crystal II, and one from "$Ba_2Cu_{3.2}Te_5$", crystal III. All three data sets gave comparable results, with refined formulas of $Ba_2Cu_{3.33(1)}Te_5$, $Ba_2Cu_{3.25(1)}Te_5$, and $Ba_2Cu_{3.23(1)}Te_5$, respectively, as summarized in Tables 3.1 and 3.2, both with respect to the Te split sites as well as the Cu deficiencies.

Table 3.1Crystallographic Data for $Ba_2Cu_{4-x}Te_5$

Refined formula	$Ba_2Cu_{3.33(1)}Te_5$, I	$Ba_2Cu_{3.25(1)}Te_5$, II	$Ba_2Cu_{3.24(1)}Te_5$, III
formula weight [g/mol]	1124.3	1118.6	1117.9
T of measurement [K]	298(2)	298(2)	298(2)
λ [Å]	0.71073	0.71073	0.71073
space group	*C*2/*c*	*C*2/*c*	*C*2/*c*
a [Å]	9.472(1)	9.4428(6)	9.4425(8)
b [Å]	9.357(1)	9.3289(6)	9.3390(7)

c [Å]	13.304(2)	13.3028(8)	13.316(1)
β [°]	101.688(3)	101.635(1)	101.567(2)
V [Å^3]	1154.7(3)	1147.8(1)	1150.4(2)
Z	4	4	4
μ [mm^{-1}]	25.06	25.05	24.98
ρ_{calcd} [g/cm^3]	6.47	6.47	6.45
$R(F_o)^a$ \ $R_w(F_o^2)^b$	0.051 \ 0.076	0.041 \ 0.063	0.043 \ 0.079

^{a} $R(F_o) = \Sigma||F_o|-|F_c|| / \Sigma|F_o|$ (all data)

^{b} $R_w(F_o^2) = [\ \Sigma[w(F_o^2 - F_c^2)^2] / \Sigma[w(F_o^2)^2]\ ]^{1/2}$ (all data)

Table 3.2 Atomic coordinates, equivalent isotropic displacement parameters and occupancy factors of $Ba_2Cu_{3.33}Te_5$.

Atom	site	x	y	z	U_{eq}/Å^2	Occ.	Occ.^{a}	Occ.^{b}
Ba	8f	0.22033(4)	0.42910(4)	0.16159(3)	0.0227(1)	1	1	1
Cu1	8f	0.0626(1)	0.0814(1)	0.07687(9)	0.0249(3)	0.692(3)	0.667(3)	0.677(3)
Cu2	8f	0.14105(9)	0.28804(8)	0.42173(6)	0.0249(2)	0.974(3)	0.956(3)	0.944(3)
Te1A	8f	0.0747(1)	0.2043(2)	0.59244(7)	0.0174(2)	0.709(5)	0.712(5)	0.716(6)
Te1B	8f	0.0936(3)	0.1669(3)	0.5920(2)	0.0174(2)	0.291	0.288	0.284
Te2A	8f	0.3490(4)	0.0704(3)	0.1040(2)	0.0175(3)	0.67(1)	0.70(1)	0.73(2)
Te2B	8f	0.3209(5)	0.0549(5)	0.1022(4)	0.0175(3)	0.33	0.30	0.27
Te3	4e	0	0.17138(5)	0.25	0.0152(1)	1	1	1

a) Occupancies of $Ba_2Cu_{3.25}Te_5$

b) Occupancies of $Ba_2Cu_{3.24}Te_5$

Next, a single crystal from the "$Ba_2Cu_{3.3}Se_{0.8}Te_{4.2}$" sample, crystal IV, was mounted on the Bruker Smart APEX. The data were collected as described for the ternary case. The unit cell dimensions were indicative of the tetragonal primitive Bravais lattice, and the systematic absences were in accord with the space groups $P4_12_12$ and $P4_32_12$. The structure solution in the former resulted in six atomic positions, tentatively assigned to be one Ba, two Cu, one Se, and two Te atoms. As above-mentioned in case of $Ba_2Cu_{3.3}Te_5$, the two Cu sites exhibited enlarged and the Te atoms significantly anisotropic thermal displacement parameters. Therefore, the Cu site occupancies were refined, and split sites for the Te sites were introduced. Then, the refinement converged with R1 = 0.034 (all data), but the Se site's thermal displacement parameter was only half of the others. Thus, that position was refined as being mixed occupied by Se and Te, resulting in an improved R1 = 0.028 (all data) and an occupancy of 73% Se and 27% Te, corresponding to the refined formula $Ba_2Cu_{3.26(2)}Se_{0.729(8)}Te_{4.271}$. The small Flack parameter of 0.11(5) indicated that the correct absolute conformation was found. As in the case of the ternary telluride, neither super cell reflections nor evidence for twinning were observed. Finally, the parameters were standardized as for the telluride.

To probe the phase range, two more crystals, V and VI, were analyzed via the Bruker Smart APEX, taken from the sample with the intermediate Se content (V, nominal composition: $Ba_2Cu_{3.3}Se_{0.25}Te_{4.75}$) as well as the smallest Se content (VI, nominal composition: $Ba_2Cu_{3.3}Se_{0.10}Te_{4.90}$). The unit cell parameters were significantly larger, indicating a smaller Se concentration, and the systematic absences pointed to the same space group, $P4_12_12$, in both cases. For crystal V, a refinement commencing from the final solution of $Ba_2Cu_{3.26}Se_{0.73}Te_{4.27}$ converged with R1 = 0.025 (all data), a Flack parameter of 0.00(7), and a refined formula of $Ba_2Cu_{3.19(1)}Se_{0.288(7)}Te_{4.712}$. The corresponding data of crystal VI were R1 = 0.024 (all data), a Flack parameter of 0.04(7), and a formula of $Ba_2Cu_{3.230(8)}Se_{0.130(5)}Te_{4.870}$. The crystallographic data of the selenide-telluride are summarized in Table 3.3, and the atomic parameters including the occupancy factors are given in Table 3.4.

To summarize, the phase range with respect to Cu is very small, the selenide-telluride adopts a different structure type, and the Se : Te ratio may vary substantially, with $0.13 \leq y \leq 1.0$ for $Ba_2Cu_{4-x}Se_yTe_{5-y}$.

Table 3.3 Crystallographic Data for $Ba_2Cu_{4-x}(Se,Te)_5$.

Refined formula	$Ba_2Cu_{3.26(2)}Se_{0.729(8)}Te_{4.271}$, IV	$Ba_2Cu_{3.19(1)}Se_{0.288(7)}Te_{4.712}$, V	$Ba_2Cu_{3.230(8)}Se_{0.130(5)}Te_{4.870}$, VI
formula weight [g/mol]	1084.3	1101.4	1111.47
T of measurement [K]	298(2)	298(2)	298(2)
λ [Å]	0.71073	0.71073	0.71073
space group	$P4_12_12$	$P4_12_12$	$P4_12_12$
a [Å]	6.5418(3)	6.6049(7)	6.6263(5)
c [Å]	25.782(2)	26.026(3)	26.045(2)
V [Å^3]	1103.3(1)	1135.4(2)	1143.6(2)
Z	4	4	4
μ [mm^{-1}]	26.61	25.43	25.22
ρ_{calcd} [g/cm^3]	6.53	6.44	6.46
$R(F_o)^a$ \ $R_w(F_o^2)^b$	0.028 \ 0.057	0.025 \ 0.045	0.024 \ 0.036

^{a} $R(F_o) = \Sigma||F_o|-|F_c|| / \Sigma|F_o|$

^{b} $R_w(F_o^2) = [\Sigma[w(F_o^2 - F_c^2)^2] / \Sigma[w(F_o^2)^2]]^{1/2}$

Table 3.4 Atomic coordinates, equivalent isotropic displacement parameters and occupancy factors of $Ba_2Cu_{3.26}Se_{0.73}Te_{4.27}$.

Atom	site	x	y	z	U_{eq}/Å^2	Occ.	Occ.^{a}	Occ.^{b}
Ba1	8*b*	0.36090(7)	0.14091(7)	0.29278(2)	0.0256(1)	1	1	1

Cu1	8*b*	0.1271(2)	0.3421(2)	0.08386(5)	0.0261(4)	0.742(4)	0.725(3)	0.733(2)
Cu2	8*b*	0.3723(2)	0.4409(2)	0.16775(4)	0.0270(3)	0.887(4)	0.870(3)	0.882(2)
Te1A	8*b*	0.0925(6)	0.1414(3)	0.17021(6)	0.0177(3)	0.72(1)	0.73(1)	0.724(9)
Te1B	8*b*	0.1436(7)	0.1290(7)	0.1691(2)	0.0177(3)	0.28	0.27	0.276
Te2A	8*b*	0.3623(2)	0.1312(7)	0.42619(4)	0.0209(3)	0.92(2)	0.79(4)	0.69(2)
Te2B	8*b*	0.356(2)	0.078(5)	0.4246(5)	0.0209(3)	0.08	0.21	0.31
Se3	4*a*	0.14439(8)	*x*	0	0.0177(2)	0.729(8)Se 0.271Te	0.288(7)Se 0.712Te	0.130(5)Se 0.870Te

a) Occupancies of $Ba_2Cu_{3.19}Se_{0.29}Te_{4.71}$

b) Occupancies of $Ba_2Cu_{3.23}Se_{0.13}Te_{4.87}$

3.3 Calculation of the electronic structure

The LMTO (linear muffin tin orbitals) method was employed with the atomic spheres approximation (ASA) for the electronic structure calculations. Therein, density functional theory is applied with the local density approximation (LDA) to treat exchange and correlation effects. The following wavefunctions were used: for Ba *6s*, *6p* (downfolded), *5d* and *4f*; for Cu *4s*, *4p*, and *3d*; for Se *4s*, *4p*, and *4d* (downfolded); and for Te *5s*, *5p*, and *5d* and *4f* (the latter two downfolded). The structural parameters were derived from the refinements II ($Ba_2Cu_{3.25}Te_5$) and IV ($Ba_2Cu_{3.26}Se_{0.73}Te_{4.27}$). Two different models were calculated for each of these two compounds because of the Te split sites: one with the majority sites filled, Te1A and Te2A, and the second with the Te1B and Te2B sites. All Cu sites were treated as fully occupied, and the mixed Se/Te position (refined as 73% Se and 27% Te) as a Se site. Therefore, the models retained the full symmetry, and the formulas $Ba_2Cu_4Te_5$ (in space group $C2/c$) and $Ba_2Cu_4SeTe_4$ (in $P4_12_12$).

For $Ba_2Cu_4Te_5$, the eigenvalue problem was solved on the basis of 172 *k* points of the irreducible wedge of the first Brillouin zone, chosen via the improved tetrahedron method. In case of $Ba_2Cu_4SeTe_4$, 474 *k* points were selected. To gain insight into the strength of various interactions, crystal orbital Hamilton populations were calculated in addition to the band structures and densities of states.

3.4 Physical Property Measurements

In case of the ternary telluride, a cold-pressed bar of the dimensions 6 × 1 × 1 mm of the sample $Ba_2Cu_{3.3}Te_{2.5}$ was prepared. The Seebeck coefficient, S, was determined via the SB100 from MMR Technologies between 300 K and 550 K, and the electrical resistivity, ρ, via a four-point-method using a home-made device between 300 K and 550 K. Silver paint (Ted Pella) was used for the electric contacts in both cases, and both measurements were carried out under dynamic vacuum.

For the selenide-tellurides, larger pellets (13 × 2 × 2 mm) of $Ba_2Cu_{3.3}Se_yTe_{5-y}$ (with y = 0.8 and 1.0) were cold-pressed and then measured utilizing the ULVAC-RIKO ZEM-3 between 300 K and 600 K. Therein, S and ρ were simultaneously determined in a helium atmosphere.

3.5 Results and Discussion

3.5.1 Crystal structures. While adopting different structure types, the crystal structures of $Ba_2Cu_{4-x}Te_5$ and $Ba_2Cu_{4-x}(Se,Te)_5$ are all comprised of chains of edge-sharing CuQ_4 tetrahedra (with *Q* = Se, Te), wherein the Cu atoms form cis/trans chains, and the Ba atoms are ninefold coordinated by the *Q* atoms (with *Q* = Se, Te). The $CuTe_4$ chains are connected via interchain Te1–Te2 interactions to puckered layers, which in turn are connected via common *Q*3 atoms to a three dimensional Cu–*Q* network. The crystal structure of $Ba_2Cu_{4-x}Te_5$ is depicted in Figure 3.1, with the Ba–Te bonds being omitted for clarity.

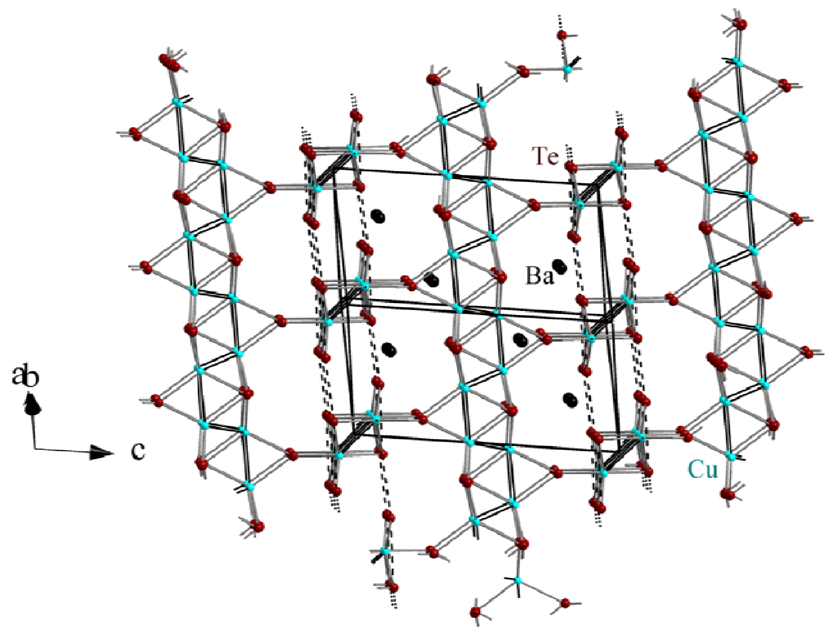

Figure 3.1 Crystal structure of $Ba_2Cu_{4-x}Te_5$.

The different symmetry of the selenide-telluride, compared to the telluride, reflects itself in a different orientation of these layers along the crystallographic *c* axis, which is twice as long in case of the selenide-telluride. The *a* and *b* axes are all around 6.6 Å for the selenide-telluride and for the telluride in the primitive setting as well. In both cases, the interconnection along *c* occurs via the Ba–*Q* bonds as well as corner-sharing of the CuQ_4 tetrahedra. The layers all run parallel to the *a*,*b* plane, and are packed along *c* according to ABAB… in case of the telluride and ABCDABCD… in case of the selenide-telluride (Figure 3. 2).

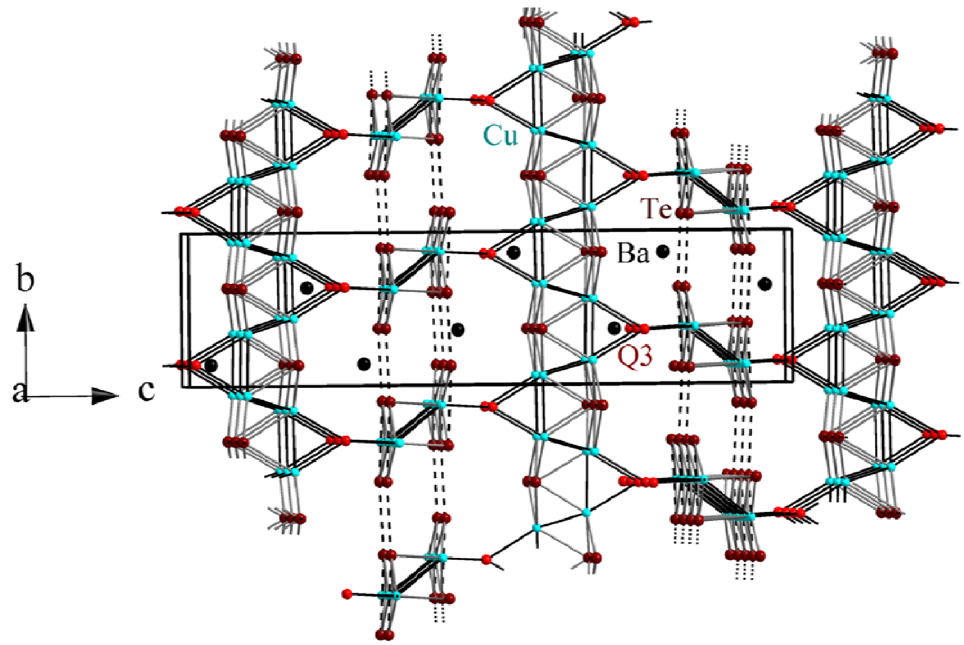

Figure 3.2 Crystal structure of $Ba_2Cu_{4-x}(Se,Te)_5$.

A striking feature of these two structure types is the occurrence of almost linear Te atom chains (which do not show any Se incorporation), depicted via the dashed lines in Figures 3. 1 and 3. 2. Therein, the Te–Te distances alternate between shorter contacts of the order of 3.0 Å and longer ones of about 3.6 Å (Figure 3. 3). Because the chains consist of the split sites of Te1 and Te2, various Te–Te distances may occur, depending on which split site is filled. For example in $Ba_2Cu_{3.19}Se_{0.29}Te_{4.71}$, the Te1A–Te2A distances are 3.03 Å and 3.58 Å, and the Te1B–Te2B 2.97 Å and 3.65 Å. The distances are almost equal in a Te1A/Te2B chain fragment with 3.32 Å and 3.28 Å, and in case of Te1B/Te2A, the separation is intermediate with 3.22 Å and 3.40 Å.

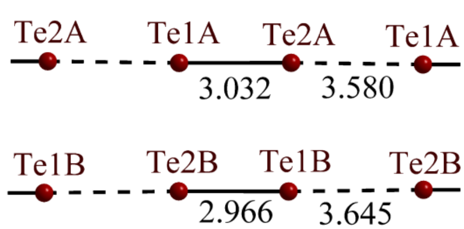

Figure 3.3 Various Te atom chains of $Ba_2Cu_{3.19}Se_{0.29}Te_{4.71}$.

The shortest of these distances resemble hypervalent (half) Te–Te bonds, as for example found in the square nets of $LaSeTe_2$ (3.05 Å),[58] the square planar Te_5^{6-} units of K_2SnTe_5 (3.02 Å and 3.05 Å)[20] or the linear center of the Te_5^{4-} fragment of Ba_2SnTe_5 (3.02 Å and 3.10 Å)[25] or NaTe (2× 3.08 Å)[59]. Treating these contacts as such half bonds and the longer ones as nonbonding, the chains may be described as infinite Te_2^{3-} chains. As the third *Q* atom, *Q*3, participates in no *Q*–*Q* contacts < 3.5 Å, it may be viewed as Q^{2-}. Then, four positive charges remain for the 4–x Cu atoms, according to $(Ba^{2+})_2Cu_{4-x}{}^{4+}Q^{2-}(Te_2{}^{3-})_2$.

This third *Q*3 site is the preferred one for the Se incorporation: at the Se-rich side of the phase range, we found no evidence for any Se contact in the Te1-Te2 chain, and 73% Se and 27% Te on the *Q*3 site. The preference of the Se atom for the site with fewer *Q*–*Q* interactions and higher formal charge is a consequence of its higher electronegativity, compared to Te, and was also observed in the structure of $LaSeTe_2$. Because of its smaller size, the Ba–*Q*3 and Cu–*Q*3 distances decrease with increasing Se content, as does the unit cell volume. For example, while all Cu–Te3 bonds in the ternary tellurides are between 2.62 Å and 2.64 Å, the corresponding distances are 2.62 Å (Cu1–*Q*3) and 2.60 Å (Cu2–*Q*3) for the case with 13% Se on *Q*3, 2.60 Å (Cu1–*Q*3) and 2.58 Å (Cu2–*Q*3) for 29% Se case, and 2.52 Å (Cu1–*Q*3) and 2.51 Å (Cu2–*Q*3) for the 73% Se case. Likewise, the unit cell volume decreases from 1151 $Å^3$, averaged over the three telluride data sets, to 1144 $Å^3$ for $Ba_2Cu_{3.23}Se_{0.13}Te_{4.87}$ and 1135 $Å^3$ for $Ba_2Cu_{3.19}Se_{0.29}Te_{4.71}$ and 1103 $Å^3$ for $Ba_2Cu_{3.26}Se_{0.73}Te_{4.27}$. The same trend was found for $Ba_3Cu_{17-x}(Se,Te)_{11}$.

The Cu atom chains exhibit Cu–Cu distances between 2.62 Å and 2.73 Å, depending on the Se content. These numbers compare well to the distances in $Ba_3Cu_{17-x}(Se,Te)_{11}$ and in $Ba_3Cu_{14-x}Te_{12}$. Interactions of these lengths are common in Cu^+ chalcogenides, and their bonding character - despite a formal $d^{10}s^0p^0$ configuration of Cu^+ - is generally understood based on hybridization effects,[60-62] as further discussed below.

Another typical observation is the significant Cu deficiency in Cu chalcogenides. In this case, a connection of the Cu deficiency with the Te split site is apparent because of the too short Cu1–Te1B and Cu1–Te2B distances (Table A.1 and A.2). For example in $Ba_2Cu_{3.33}Te_5$, the distances are 2.35 Å and 2.41 Å, respectively, significantly shorter than the regular Cu–Te distances of 2.6 Å – 2.7 Å, and the occupancies were refined to 74% for Cu1 (i.e., a deficiency of 26%), 28% for Te1B, and 8% for Te2B. One may thus assume that the Cu deficiency causes the Te split sites, i.e. the ideal position of these Te atoms depend on whether or not a neighboring Cu1 atom is present.

3.5.2 Electronic structures. The densities of states, DOS, of the two *$Ba_2Cu_4Te_5$* models A (based on Te1A and Te2A) and B (based on Te1B and Te2B) are compared in Figure 3. 4. In both cases, a distinct pseudo band gap appears at the Fermi level, E_F, where the states are dominated by the Te1 and Te2 contributions. The Cu *3d* states dominate the area between –2 eV and –5 eV.

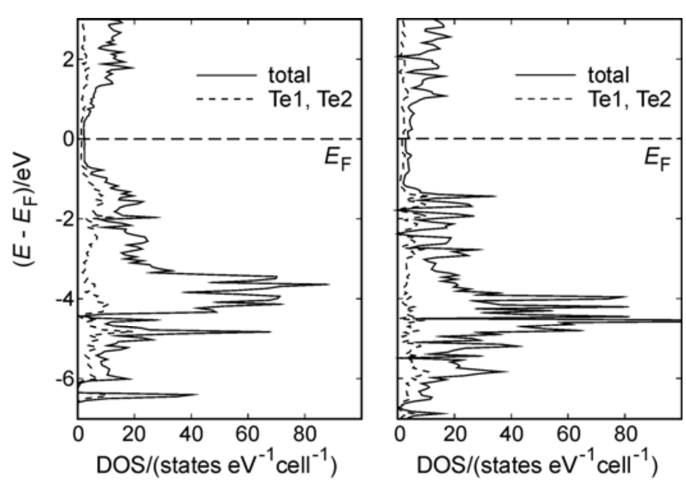

Figure 3.4 Densities of states (DOS) of the $Ba_2Cu_4Te_5$ models. Left: model A, using Te1A and Te2A; right: model B, using Te1B and Te2B.

The densities of states of two *$Ba_2Cu_4SeTe_4$* models show very similar features, e.g. the pseudo gap and the Cu *d* peaks. The absence of a band gap in the vicinity of E_F distinguishes these materials from the other Ba-Cu chalcogenides studied by us so far: $Ba_3Cu_{14-x}Te_{12}$, $Ba_{6.76}Cu_{2.42}Te_{14}$, $Ba_2(Cu,Ag)_4Se_5$[63], $Ba(Cu,Ag)_2Te_2$, and $Ba_3Cu_{17-x}(Se,Te)_{11}$ all exhibit such gaps and are *p*-type semiconductors.

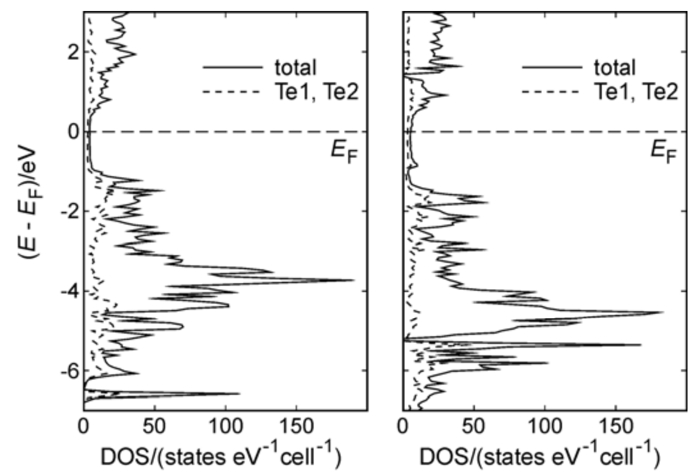

Figure 3.5 Densities of states (DOS) of the $Ba_2Cu_4SeTe_4$ models. Left: model A, using Te1A and Te2A; right: model B, using Te1B and Te2B.

The p_x and p_y contributions of the Te atoms of the quasi-linear Te chains, that run parallel to both the *a* and the *b* axis of the selenide-telluride, cause the absence of the energy gap, as demonstrated via the fat band[64] representation (Figure 3.6). The bands originating from these orbitals cross E_F in the *a**, *b** plane with large dispersions, while no bands cross E_F parallel to *c**. Such a scenario is indicative for two-dimensional metallic properties. With the experimentally observed Cu deficiency of x ≈ 0.75, one can approximate that the actual electron count is 0.75 electrons less per formula unit, when Cu is in its +1 state. This would lower the Fermi level by 0.7 eV in the case of the telluride as well as selenide-telluride, i.e. into an area that is still dominated by the steep bands of the p_x and p_y contributions of the Te atoms of the quasi-linear Te chains.

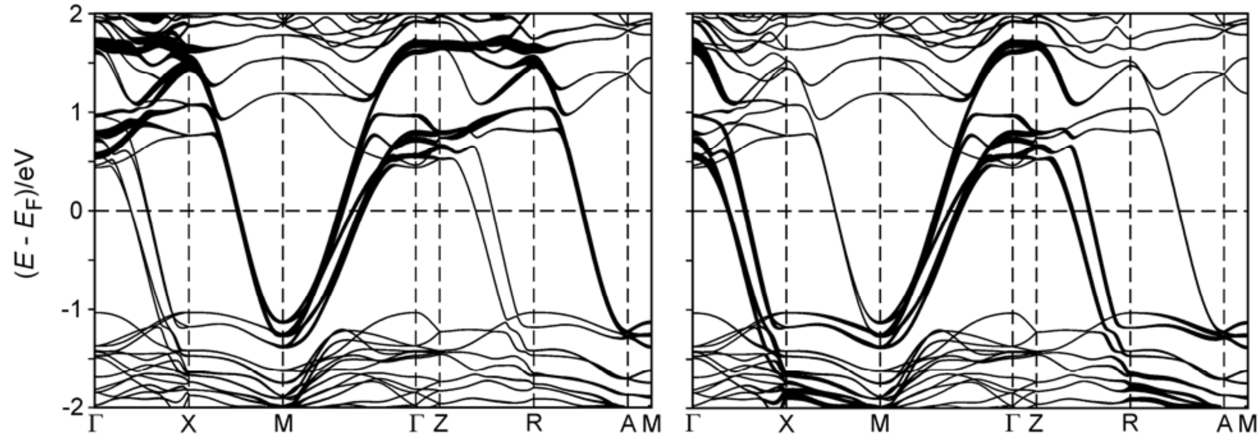

Figure 3.6 Band structure of the $Ba_2Cu_4SeTe_4$ model A. Left: emphasis of the px contributions of Te1A and Te2A; right: py. Γ: (0, 0, 0); X: (0, 0.5, 0); M: (0.5, 0.5, 0); Z: (0, 0, 0.5); R: (0, 0.5, 0.5); A: (0.5, 0.5, 0.5) - in fractional coordinates of the reciprocal lattice.

The crystal orbital Hamilton population curves computed for model A of *$Ba_2Cu_4SeTe_4$* demonstrate that no Cu–*Q* or Cu–Cu bonds contribute to the states around E_F. Both the Cu–Se and Cu–Te bonds are optimized, as the Fermi level separates the filled bonding from the empty antibonding states. Most of the strength of the Cu–Cu bonds comes from the strongly bonding peak at –6.5 eV, which also occurs within the Cu–*Q* interactions. The largest contribution to this peak comes from the p_z orbitals of Se3, covalently mixing with the *s* orbitals of both Cu sites. This in turn explains why Cu–Cu bonding occurs despite the normally assumed d^{10} configuration. While the Cu–Cu bonds also exhibit basically no states at E_F and almost exclusively bonding states below E_F, the states in the region up to 1.5 eV above E_F are bonding as well. Hence, an increase in the valence electron concentration would occur with weakened Cu–*Q*, but strengthened Cu–Cu interactions, while a decrease - as experimentally observed because of the Cu deficiency - would weaken all these interactions by depopulating bonding states.

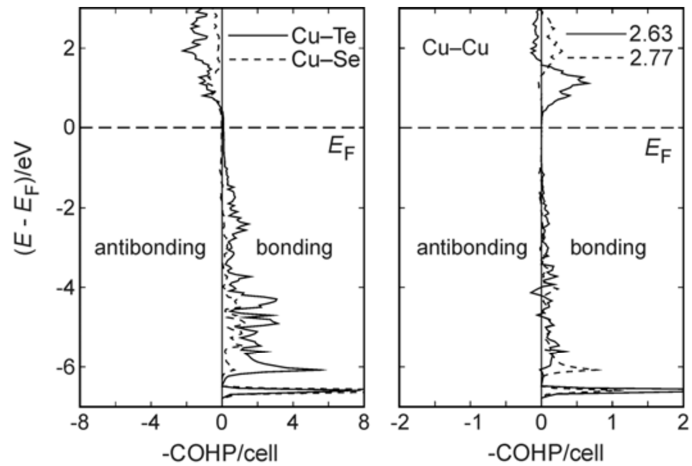

Figure 3.7 Selected cumulated crystal orbital Hamilton population (COHP) curves of the $Ba_2Cu_4SeTe_4$ model A. Left: Cu–Q; right: Cu–Cu.

On the other hand, both different Te1A–Te2A and both different Te1B–Te2B interactions of $Ba_2Cu_4SeTe_4$ become antibonding well below E_F, and have a significant contribution directly at E_F. Therefore, a smaller valence electron concentration would lead to stronger Te–Te bonds. In the model $Ba_2Cu_4SeTe_4$, the shorter ones of 3.02 Å (Te1A–Te2A) and 2.85 Å (Te1B–Te2B) are significantly bonding with integrated COHP values, ICOHP,[65] of –0.46 eV and –0.29 eV, respectively. Here, the shorter interaction is the weaker bond, because more antibonding states are filled. The two longer interactions of 3.53 Å and 3.71 Å are basically net nonbonding, with ICOHP values of 0.06 eV and –0.01 eV.

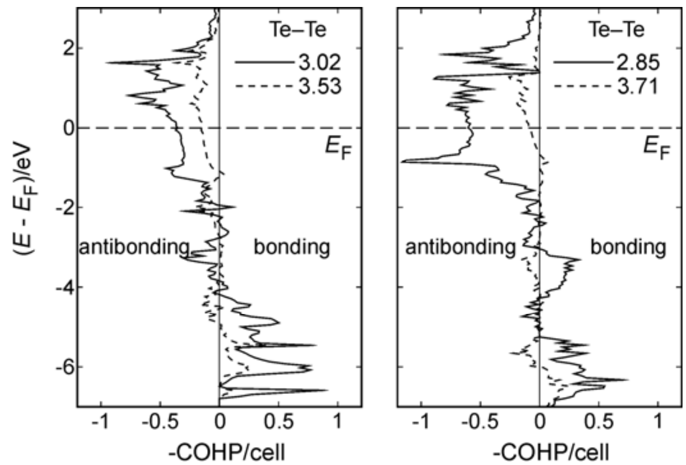

Figure 3.8 Te–Te crystal orbital Hamilton population (COHP) curves of the $Ba_2Cu_4SeTe_4$ models A (left) and B (right).

3.5.3 Physical properties. Although the band structure calculations pointed towards two-dimensional metallic character, $Ba_2Cu_{3.3}Se_yTe_{5-y}$ with y = 0, 0.8, 1.0 were all determined to be *p*-type semiconductors with large Seebeck coefficient values, S. S decreases with increasing Se content, e.g. at 300 K from +440 μVK^{-1} for y = 0 to +340 μVK^{-1} for y = 0.8 and to +310 μVK^{-1} for y = 1.0. In all three cases, S decreases with increasing temperature, e.g. from 300 K to 500 K down to +170 μVK^{-1} for y = 0 (Figure 3. 9).

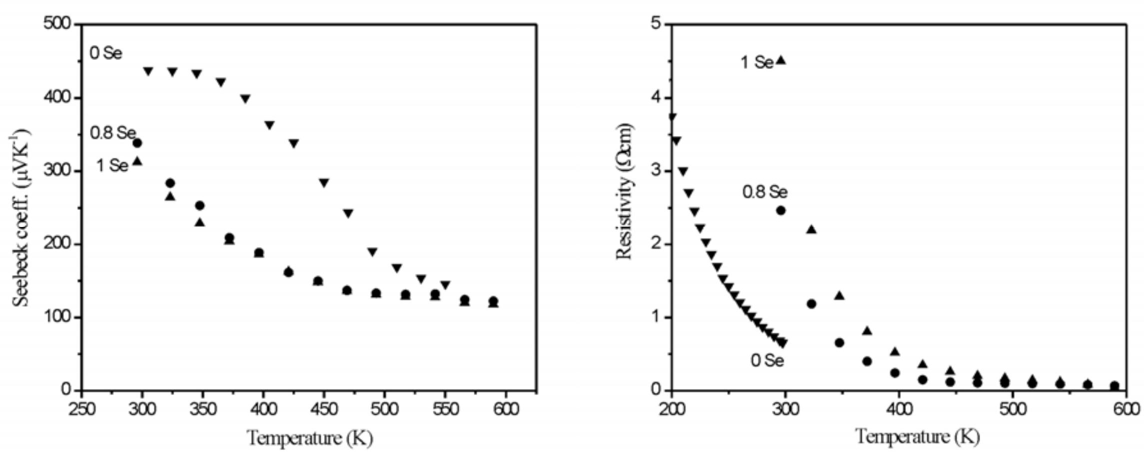

Figure 3.9 Seebeck coefficient (left) and electrical resistivity (right) of $Ba_2Cu_{3.3}Se_yTe_{5-y}$.

The electrical resistivity, ρ, decreases almost exponentially with increasing temperature, as is typical for extrinsic semiconductors. ρ increases with increasing y within the series $Ba_2Cu_{3.3}Se_yTe_{5-y}$: at 300 K, the values are 0.65 Ωcm for y = 0, 2.5 Ωcm for y = 0.8, and 4.5 Ωcm for y = 1.0. At 500 K, all values have fallen below 0.2 Ωcm. The increase of ρ with increasing Se concentration is expected for a semiconducting selenide-telluride, for the band gap increases with increasing Se because of its higher electronegativity, which lowers the valence band.[66]

3.6 Conclusions

Two new structure types were uncovered, one adopted by the telluride $Ba_2Cu_{4-x}Te_5$ and the other by the selenide-telluride $Ba_2Cu_{4-x}Se_yTe_{5-y}$. Therein, x may vary at least within $0.67 \leq x \leq 0.81$, and y within $0.13 \leq y \leq 1.0$. Both structures are comprised of the same structure motifs, but exhibit a different long range order. The structures include unusual Te atom chains with alternating short distances of the order of 3.0 Å and long ones of the order of 3.6 Å. The former are bonding, albeit being longer than typical Te–Te single bonds, and the latter are basically nonbonding, because the filled bonding states are matched by the filled antibonding states. Both Cu sites exhibit significant deficiencies in all cases, which appear to be connected to the split sites of the two independent Te atoms of the Te atom chains.

The fact that these materials are semiconductors - as experimentally determined - in contrast to the calculated band structures, implies that the models chosen for the calculations were not close enough to the reality, considering the various split sites combined with the Cu atom deficiencies. The calculated band structures indicated two-dimensional metallic properties caused by the Te–Te interactions, which should be prone to undergo a Peierls distortion.

Chapter 4 Structure and properties of new quaternary compounds $Ba_2Cu_{6-x}Q_5$

4.1 Syntheses and Analyses

The new sulfide-telluride, $Ba_2Cu_{5.53}STe_4$ was first obtained in an attempt to prepare a compound of the nominal composition "BaCuSTe", while trying to investigate the existence of nonclassical bonding in chalcogenides. The respective elements were loaded into a fused silica tube in an argon-filled glove box followed by sealing under vacuum. The fused tube was heated to 800°C within 32 hours, and kept at that temperature for two days and then cooled down to 400°C at the rate of 1°C per hour, followed by switching off the furnace. A suitable single crystal was picked from the sample for single crystal X-ray diffraction. Solving the structure by single crystal X-ray determination proved the compound to be of a new structure type with stoichiometry, $Ba_2Cu_{6-x}STe_4$ ($x = 0.5$), as explained in the succeeding section. The phase pure samples were prepared using the same temperature profile starting from the stoichiometry 2:5.5:1:4 (Ba: Cu: S: Te). Thererafter the products were ground and analyzed by using powder X-ray diffraction. The powder XRD pattern of the sample indicated that the sample is single phase when compared with the simulated pattern from the cif data file (Figure 4.1).

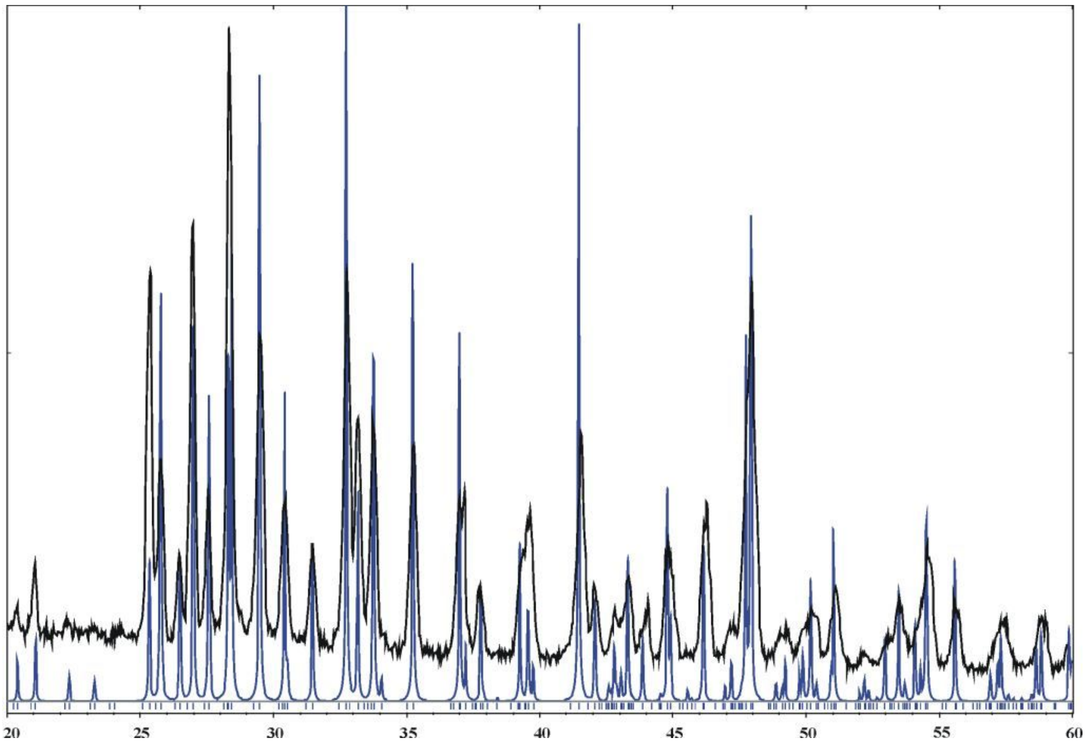

Figure 4.1 Experimental (Black) and simulated (Blue) XRD pattern of $Ba_2Cu_{5.5}STe_4$.

Attempts were made to synthesize isostructural compounds with varying chalcogen atoms and with different coinage metals. However, substitution of Cu by Ag or Au was not possible when synthesis was attempted with the above mentioned conditions. Reactions of nominal compositions $Ba_2Cu_{5.5}Te_5$ and $Ba_2Cu_{5.5}SSe_4$ gave XRD patterns with $BaCu_2Te_2$[32] and $BaCu_2Se_2$[67] (1–2–2 type compounds) as major phases respectively, under the same reaction conditions. More reactions with stoichiometries similar to $Ba_2Cu_{5.5}Q_5$ (Q = S, Se, Te) gave mostly their respective (1–2–2) compounds. A reaction with Se substituting the S atom of $Ba_2Cu_{5.5}STe_4$, starting with exactly similar stoichiometry of elements ("$Ba_2Cu_{5.5}SeTe_4$") was successful. The single crystal X-ray data of this compound yielded a refined formula of $Ba_2Cu_{5.64}Se_{1.09}Te_{3.91}$ (Table 4.1). The pure compound was synthesized with the same temperature profile mentioned above and its powder XRD pattern compared with the simulated pattern from single crystal XRD studies (Figure 4.2).

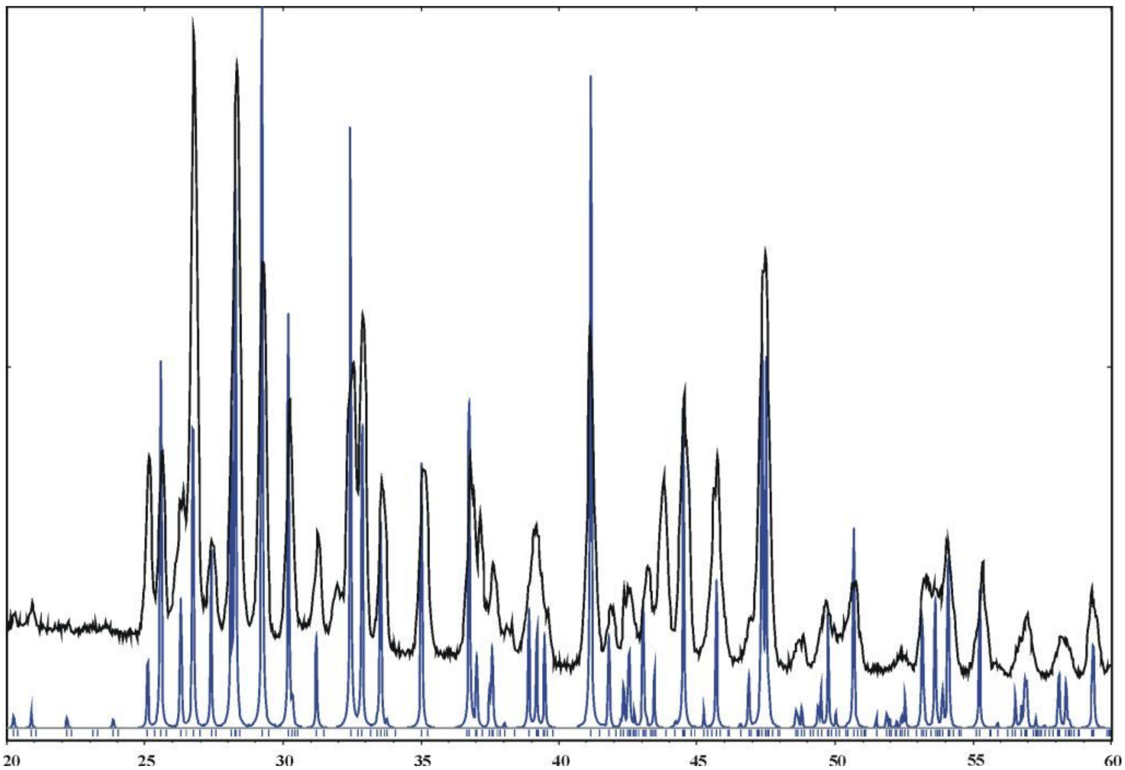

Figure 4.2 Experimental (Black) and simulated (Blue) XRD pattern of $Ba_2Cu_{5.64}Se_{1.09}Te_{3.91}$.

Phase range studies on $Ba_2Cu_{5.64}Se_yTe_{5-y}$, were carried out by varying y. When y >2, different products form, according to our powder XRD studies. The reaction with y=2, i.e. of nominal composition $Ba_2Cu_{5.7}Se_2Te_3$, was found to have a similar powder XRD pattern with a slight shift towards higher angles compared with $Ba_2Cu_{5.64}Se_{1.09}Te_{3.91}$ which is expected (Figure A.1 in appendix), when Te is substituted by smaller Se within the structure. Substitution with Se between $0 < y < 1$ in $Ba_2Cu_{6-x}Se_yTe_{5-y}$ is currently underway.

Table 4.1 Crystallographic Data for $Ba_2Cu_{6-x}Q_5$.

Refined formula	$Ba_2Cu_{5.53}STe_4$	$Ba_2Cu_{5.64}Se_{1.09}Te_{3.91}$
formula weight [g/mol]	1167.25	1217.78
T of measurement [K]	296(2)	296(2)
λ [Å]	0.71073	0.71073

).

space group	*Pbam*	*Pbam*
a [Å]	9.6560(6)	9.7048(6)
b [Å]	14.0533(9)	14.1853(9)
c [Å]	4.3524(3)	4.3840(3)
V [Å^3]	590.61(7)	603.53(7)
Z	2	2
μ [mm^{-1}]	26.08	28.65
ρ_{calcd} [g/cm^3]	6.564	6.701
$R(F_o)^a$ \ $R_w(F_o^2)^b$	0.0265 \ 0.0634	0.0212 \ 0.0440

Energy dispersive X-ray analyses, using a scanning electron microscope with an additional EDX device, were carried out on these samples. The atomic percentages of $Ba_2Cu_{5.5}STe_4$, averaged over eight crystals were measured to be 15.5: 44.9: 8.1: 31.5 for the quaternary sulfur telluride and 15.9: 45.5: 10.2: 28.3 for the selenium telluride, which agree reasonably well with the expected ratio (16.0: 44.1: 8.0: 31.9), Table. 4.2.

Table 4.2 EDX data of $Ba_2Cu_{5.53}STe_4$.

	At-%	overall	1	2	3	4	5	6	7	8	Average
Ba L	15.96	14.86	15.73	15.40	15.62	15.65	15.52	14.81	15.75	15.77	15.53
Cu K	44.13	46.73	46.15	44.23	45.08	43.99	43.95	47.20	44.65	43.84	44.89
S K	7.98	7.21	6.38	9.00	8.58	8.79	8.70	6.52	8.05	8.99	8.13
Te L	31.92	31.20	31.73	31.37	30.72	31.57	31.83	31.47	31.55	31.4	31.46

Differential scanning calorimetry (DSC) measurements on these samples showed the melting points as 790ºC and 778ºC for $Ba_2Cu_{5.53}STe_4$ and $Ba_2Cu_{5.64}SeTe_4$, respectively (Figure 4.3).

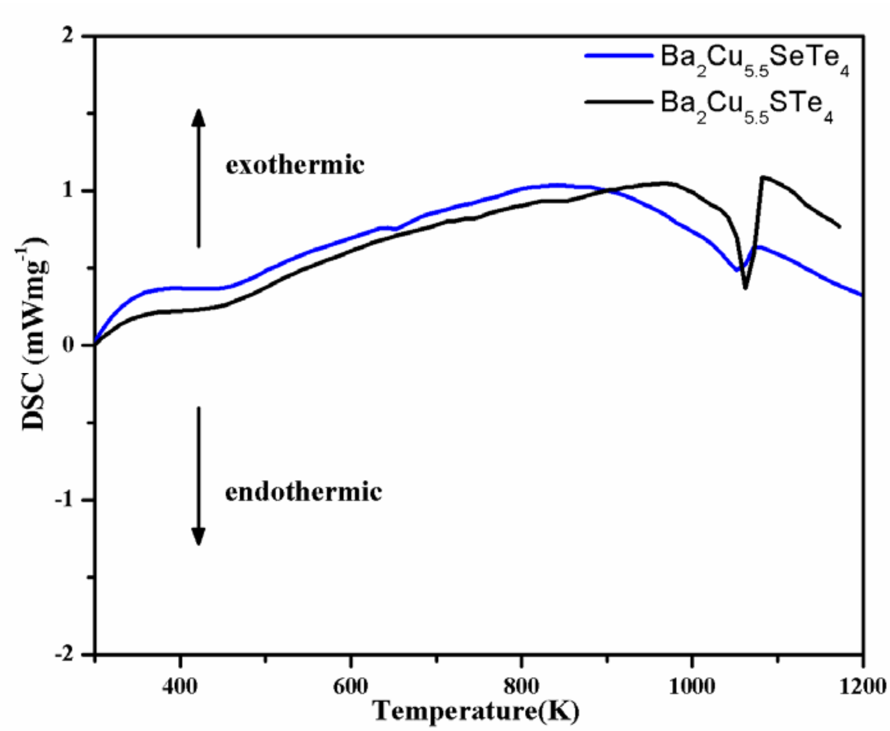

Figure 4.3 DSC curves of $Ba_2Cu_{5.64}SeTe_4$ and $Ba_2Cu_{5.53}STe_4$.

4.2 Structure determination

A black, plate like single crystal of the nominal composition "BaCuSTe" was selected for the structure determination. For this, 606 frames were measured with each frame exposed for 60 seconds to the radiation. The data were corrected for Lorentz and polarization effects. Unit cell parameters indicated orthorhombic symmetry. The structure was refined using SHELXTL program package as mentioned before. The systematic absences restricted the possible space group to the space groups *Pba*2 *and Pbam*. Using the "Direct Method" of SHELXS in the space group *Pbam* yielded a total of seven atomic sites, one Ba, three Cu, one S and two Te atoms. The occupancy factors of the Cu sites were further refined, since the refinement yielded large thermal expansion parameters in case of the three Cu sites, most notably so for Cu2, thereby yielding deficiencies of 3% (Cu1), 19% (Cu2), and 2% (Cu3), and an R1 value of 0.0265, compared to 0.0357 for the refinement with fully occupied Cu sites (Table 4.3). The Cu2 atom shows an elongated U_{22} parameter, approximately three times larger than the average of the U_{11} and U_{33}. Introducing split sites to Cu2 tentatively failed to improve the anisotropic parameters. So the refinement without splits was considered as final. With the help of PLATON program, all atomic positions were standardized.

In the case of selenide-telluride, the crystal structure was refined similarly. The refinement yielded similar Cu deficiencies of 4% (Cu1), 13% (Cu2), and 1% (Cu3). Because of the high U values of Te2, that site was refined as being mixed occupied by Se and Te, resulting in an improvement of R1 from 0.0217 to 0.0212. The atomic coordinates are shown in Table 4.4.

Table 4.3 Atomic coordinates, equivalent isotropic displacement parameters and occupancy factors of $Ba_2Cu_{5.51(3)}STe_4$.

Atom	Site	*x*	*y*	*z*	U_{eq}/Å^2	occ.
Ba1	4*h*	0.02298(4)	0.16049(3)	1/2	0.01378(16)	1
Cu1	4*h*	0.38707(11)	0.09261(8)	1/2	0.0226(4)	0.971(5)
Cu2	4*g*	0.02736(14)	0.40999(14)	0	0.0363(6)	0.805(6)
Cu3	4*g*	0.24614(10)	0.00997(8)	0	0.0216(3)	0.978(4)
S1	2*a*	0	0	0	0.0130(5)	1
Te1	4*h*	0.17436(5)	0.40777(4)	1/2	0.01446(16)	1
Te2	4*g*	0.30984(4)	0.19612(4)	0	0.01281(16)	1

Table 4.4 Atomic coordinates, equivalent isotropic displacement parameters and occupancy factors of $Ba_2Cu_{5.64(3)}Se_{1.098(4)}Te_{3.902}$.

Atom	site	*x*	*y*	*z*	U_{eq}/Å^2	occ.
Ba1	4*h*	0.02464(4)	0.16610(3)	1/2	0.01483(11)	1
Cu1	4*h*	0.38658(10)	0.09305(6)	1/2	0.0229(3)	0.960(4)
Cu2	4*g*	0.02614(11)	0.40792(8)	0	0.0253(4)	0.866(5)
Cu3	4*g*	0.25683(9)	0.01335(6)	0	0.0210(3)	0.993(4)

Se1	2*a*	0	0	0	0.01292(17)	1
Te1	4*h*	0.17468(4)	0.40932(3)	1/2	0.01315(11)	1
Te2	4*g*	0.31031(4)	0.19748(3)	0	0.01259(13)	0.951(2)
Se2	4*g*	0.31031(4)	0.19748(3)	0	0.01259(13)	0.049

4.3 Electronic Structure Calculations

LMTO calculations were done on these compounds. In both cases, all three copper sites were considered as fully occupied and in case of selenide–telluride, although the *Q*2 site is mixed occupied with 5% Se and 95% Te, full Te occupancy was considered while choosing the model. So the formulas of the models are $Ba_2Cu_6STe_4$ and $Ba_2Cu_6SeTe_4$. 455*k* points of the irreducible wedge of the first Brillouin zone were chosen for calculations.

4.4. Results and Discussion

4.4.1 Crystal Structures. Two new quaternary chalcogenides, $Ba_2Cu_{5.53}STe_4$ and $Ba_2Cu_{5.64}Se_{1.09}Te_{3.91}$, crystallize in the orthorhombic crystal system with space group *Pbam*. These structures are comprised of Cu_6 units extending along the *c* axis throughout the crystal (Figure 4.4). Here, the Cu–Cu contacts vary from 2.56 Å to 2.93 Å; similar Cu–Cu distances were found in $Ba_3Cu_{14-x}Te_{12}$ [34]and $Ba_3Cu_{17-x}Se_{11-y}Te_y$[37]. In $Ba_2Cu_{5.53}STe_4$, two such extended units are interconnected along *a* axis with S atoms, and Cu1 and Cu3 form a distorted tetrahedron with the chalcogen atoms. Cu1 is bonded to two Te1 atoms with 2.78 Å and 2.66 Å and two Te2 atoms with the distance of 2.72 Å. Similarly, Cu3 is also coordinated with two Te1, S1 and one Te2 with distances 2.72 Å, 2.38 Å, and 2.69 Å, respectively. On the other hand, Cu2 forms almost planar $CuTe_3$ units, as also found in $Ba_3Cu_{14-x}Te_{12}$ and $Ba_3Cu_2Sn_3Se_{10}$,[68] which extend along the *c* axis sharing Te1 using two Te1 and one Te2 atoms with distances 2.60 Å and 2.58 Å, respectively. In $Ba_2Cu_{5.64}Se_{1.09}Te_{3.91}$, the Se atoms are holding the extended copper units and the Cu–Se/Te distances are different from that of

$Ba_2Cu_{5.53}STe_4$, though the coordination polyhedra are topologically equivalent. Cu1 is coordinated by two Te1 atoms with 2.80 Å and 2.67 Å and two Te2/Se2 with distances 2.75 Å. Similarly, Cu3 is also coordinated by two Te1, Se1 and one Te2/Se2 with distances 2.73 Å, 2.50 Å, and 2.66 Å, respectively, and Cu2 forms similar $CuTe_3$ units with two Te1 and one Te2/Se2 atoms with distances 2.62 Å and 2.57 Å, respectively (Table A.3). In this compound, Te is in (-2) oxidation state and forms no *Q*–*Q* bond whereas *Q*–*Q* bonds exists in case of $Ba_2Cu_{4-x}(Se, Te)_5$,[69] explained in the previous chapter.

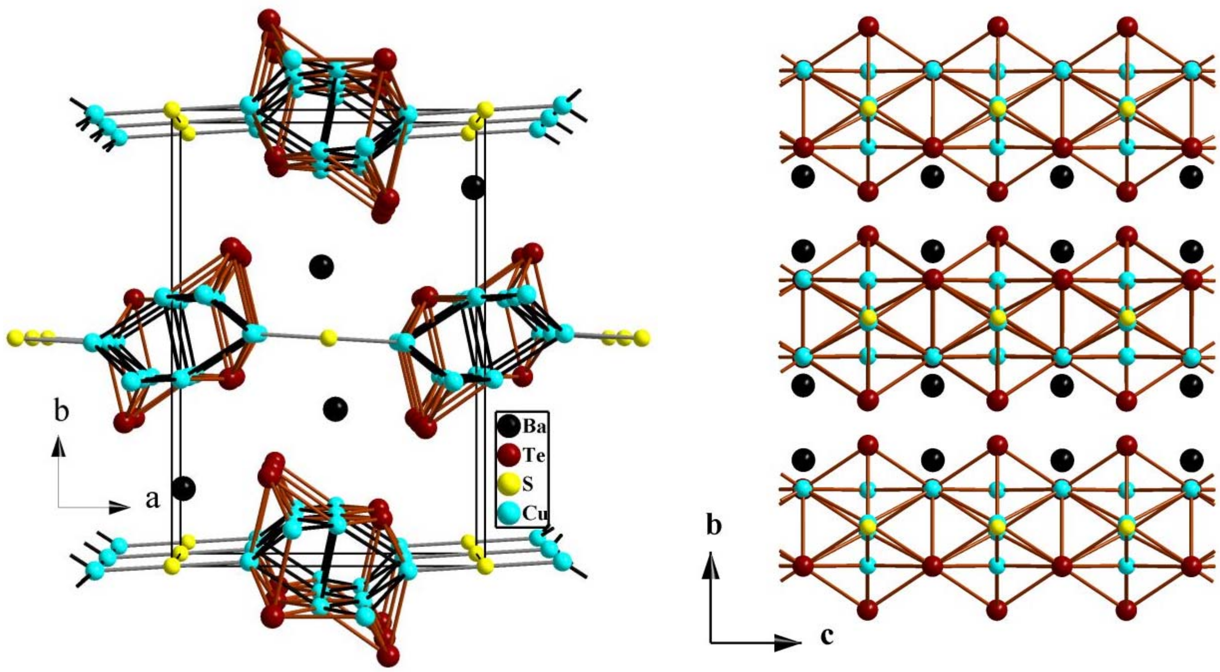

Figure 4.4 Crystal structure of $Ba_2Cu_{6-x}STe_4$.

4.4.2 Electronic Structure Calculations. The total DOS and the contributions of the Cu-*d* states of the models $Ba_2Cu_6STe_4$ and $Ba_2Cu_6SeTe_4$ are compared in Figure 4.5. A very narrow gap separates the valence band, which is dominated by the Cu-*d* states, from the conduction band in case of the selenides-telluride, while the two bands touch in case of the sulfide-telluride.

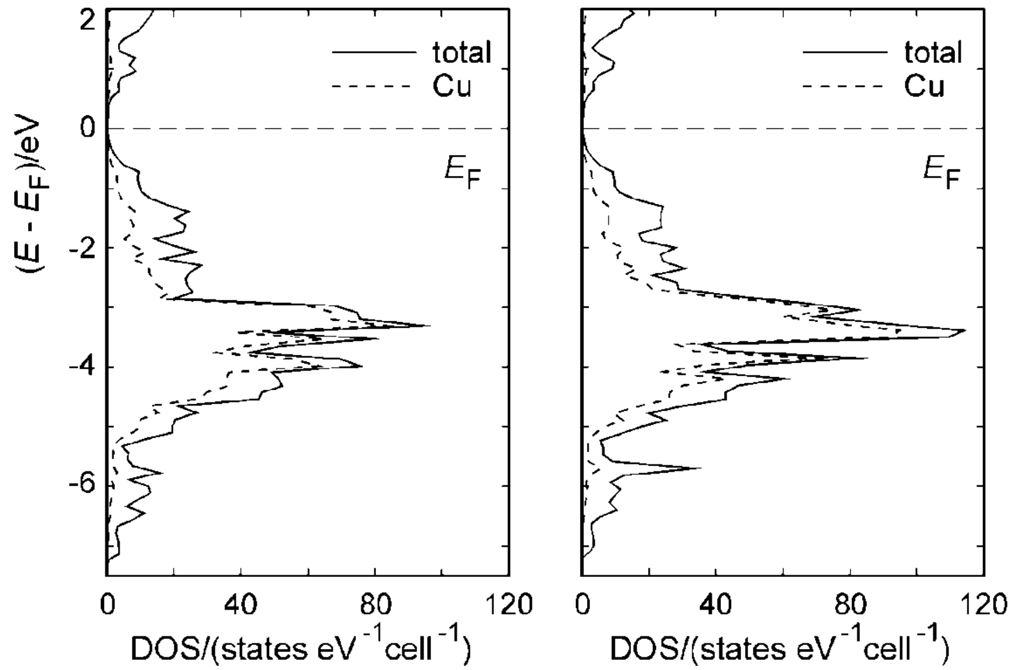

Figure 4.5 Densities of states (DOS) of (a) $Ba_2Cu_6STe_4$ (b) $Ba_2Cu_6SeTe_4$ model.

The band structures (Figure 4.6), reveal that the band gap is in indirect one in both cases. The maximum of the valence band occurs at the Γ point, and the minimum of the conduction band at the Z point, touching the Fermi level in case of the sulfide.

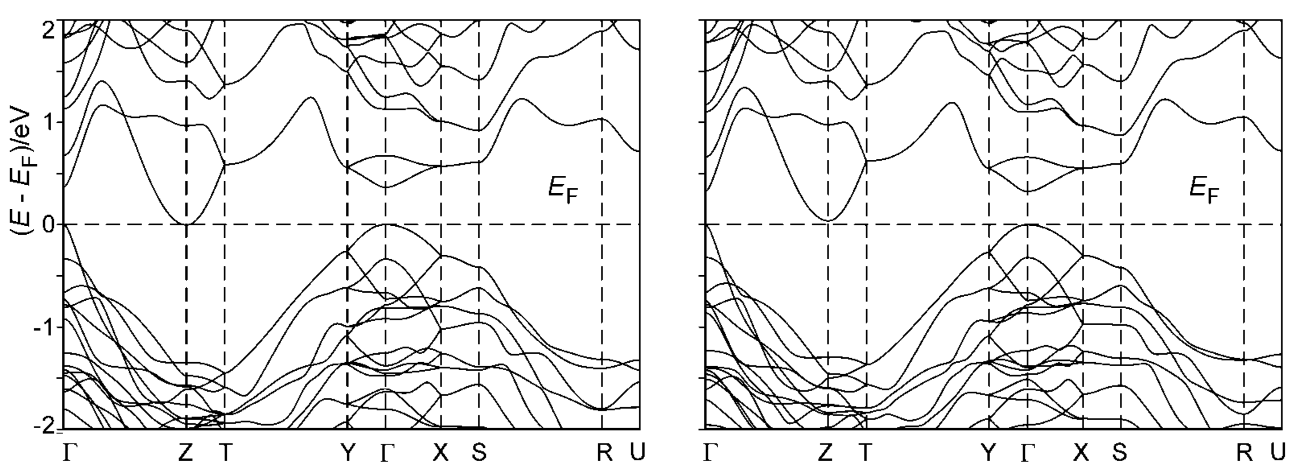

Figure 4.6 Band structure of (a) $Ba_2Cu_6STe_4$ (b) $Ba_2Cu_6SeTe_4$ model: Γ: (0, 0, 0); Z: (0, 0, 0.5); T: (0, 0.5, 0.5); Y: (0, 0.5, 0); X: (0.5, 0, 0); S: (0.5, 0.5, 0); R: (0.5, 0.5, 0.5); U: (0.5, 0, 0.5) - in fractional coordinates of the reciprocal lattice.

4.5 Physical property measurements

Phase pure samples were cold-pressed in the shape of bars of the dimensions 13x 2x 2 mm^3, which were then used to measure electrical conductivity (σ) and Seebeck coefficient (S) simultaneously between 300 K and 600 K, with the help of ULVAC-RIKO ZEM-3.

The physical property measurements on $Ba_2Cu_{5.53}STe_4$, $Ba_2Cu_{5.53}SeTe_4$ and $Ba_2Cu_{5.64}Se_yTe_{5-y}$ (y = 1.1, 2) samples showed nonmetallic behavior, ie, decreasing resistivity with increasing temperature. The resistivity plots don't seem to be really exponential. Seebeck measurements also showed *p*-type behavior (Figure 4.7). The resistivity was found to decrease with increasing y in $Ba_2Cu_{5.64}Se_yTe_{5-y}$ whereas Seebeck increases with increasing Se concentration.

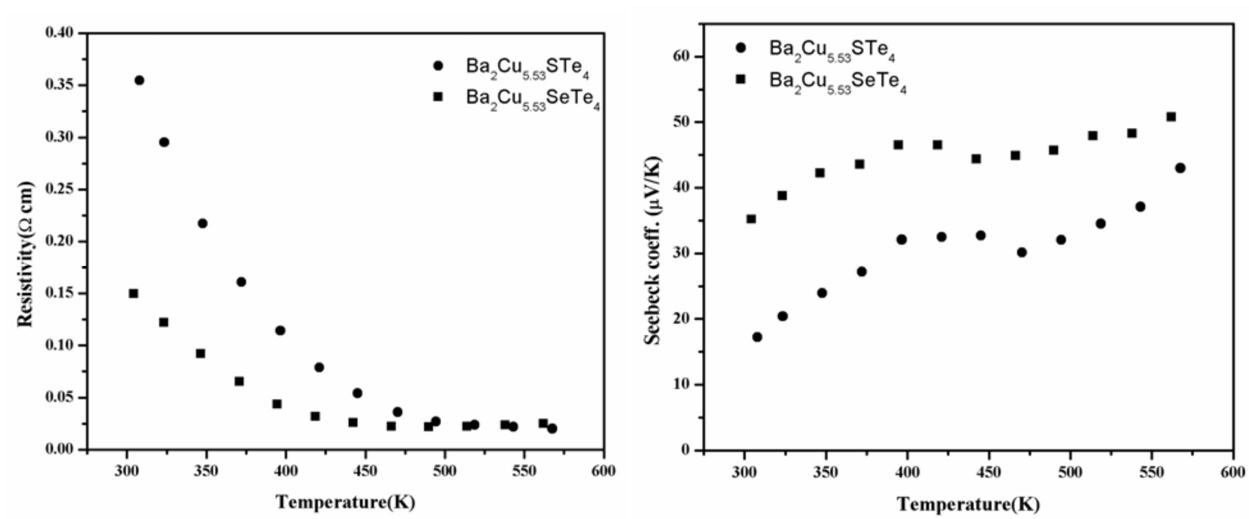

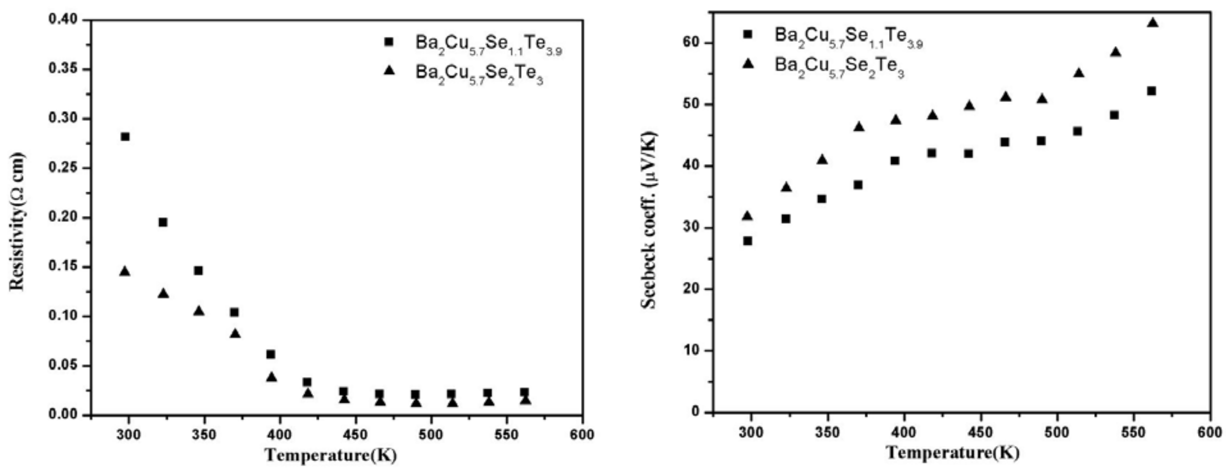

Figure 4.7 Electrical resistivity (left) and Seebeck coefficient (right) of (a) $Ba_2Cu_{5.53}STe_4$ and $Ba_2Cu_{5.53}SeTe_4$ (b) $Ba_2Cu_{5.7}Se_yTe_{5-y}$.

4.6 Conclusions

Two new compounds $Ba_2Cu_{5.53}STe_5$ and $Ba_2Cu_{5.64}Se_yTe_{5-y}$ ($y \leq 2$) with a new structure type were uncovered. All the three Cu sites exhibit significant deficiencies in these two cases. Reactions performed to find more isostructural compounds by substituting with different chalcogen atoms were unsuccessful (Table A.4). Substituting more Se in $Ba_2Cu_{5.53}Se_yTe_{5-y}$ were successful till y = 2 by following the same reaction conditions. More reactions can be done in future in these series of compounds by with varying ‘x’ in $Ba_2Cu_{6-x}(Se_yTe_{5-y})$ and $Ba_2Cu_{6-x}STe_4$.

Physical properties measured on these samples showed low Seebeck coefficient and nonmetallic behavior, while the band structure calculations using LMTO predicted semimetallic nature for the sulfide and semiconducting for the selenide.

Chapter 5 Structure and Properties of the new Selenium-Telluride $BaCu_{8-x}(Se, Te)_7$

During our study on heavy metal copper chalcogenides, we uncovered several new materials, some of them belonging to new structure types, such as $Ba_3Cu_2Sn_3Se_{10}$, $Ba_3Cu_{14-\delta}Te_{12}$, $Ba_{6.76}Cu_{2.42}Te_{14}$, $Ba_2Cu_4Te_5$, $Ba_2Cu_{4-\delta}(Se, Te)_5$, $Ba_3Cu_{17-\delta}(Se, Te)_{11}$ etc. Many of these copper containing chalcogenides exhibit interesting structural characteristics and non-classical bonding. Some interesting structural features in such heavy metal copper chalcogenides to be mentioned here are, linear Se_3^{4-} units in $Ba_2Cu_\delta Ag_{4-\delta}Se_5$, bent Te_3^{2-} units in $Ba_{6.76}Cu_{2.42}Te_{14}$ and $Ba_7Au_2Te_{14}$, Cu atom cis/trans chain and pseudo linear Te-atom chain in $Ba_2Cu_{4-\delta}Te_5$ and $Ba_2Cu_{4-\delta}(Se, Te)_5$ with $0.67(1) \leq \delta \leq 0.81(1)$, Cu_{26} clusters in $Ba_3Cu_{17-\delta}(Se, Te)_{11}$, Cu_8Te_{12} pentagonal dodecahedral cage cluster in $K_4Cu_8Te_{11}$[70], $A_3Cu_8Te_{10}$ (A= Rb, Cs), $AA'_2Cu_8Te_{10}$ (A, A′= K, Rb, Cs)[71] and $A_2BaCu_8Te_{10}$ (A= K, Rb, Cs)[33] etc. We have already seen two new structure types with interesting structural features in previous two chapters. Another two new compounds, $BaCu_{5.9}SeTe_6$ and $BaCu_{5.6}Se_{0.46}Te_{6.54}$ with such a special feature are described in this chapter.

5.1 Syntheses and Analyses

The quaternary selenide- telluride was obtained in an attempt to prepare compound of the nominal composition "$Ba_4Cu_{7.6}Q_{13}$ (Q = Se, Te)". The samples were prepared from their constituent elements of the purity mentioned in the second chapter. The mixture of elements in the quartz ampoule was heated up to a maximum temperature of 800°C in 6 hours then cooled down to 300ºC within 200 hours, and finally the furnace was switched off. Suitable single crystals were picked from the reaction mixture for the single crystal X-ray studies. The details of the single crystal X-ray analyses are given in the succeeding section. The pure compounds were obtained by heating the quartz tube containing constituent elements up to 500°C in 24 hours followed by cooling down to 400°C within 200 hours and finally to room temperature. The sample was ground and annealed further at 390°C for 240 hours.

Several attempts to synthesize phase pure $BaCu_{5.9}SeTe_6$ and $BaCu_{5.6}Se_{0.46}Te_{6.54}$ resulted in almost pure compounds, containing elemental tellurium as a minor second phase, identified using powder X-ray diffractometer, (peak of ~5% intensity in XRD pattern at $2\theta \approx 28°$) for $BaCu_{5.9}SeTe_6$, Figure 5.1. Phase range studies done on these samples were not successful.

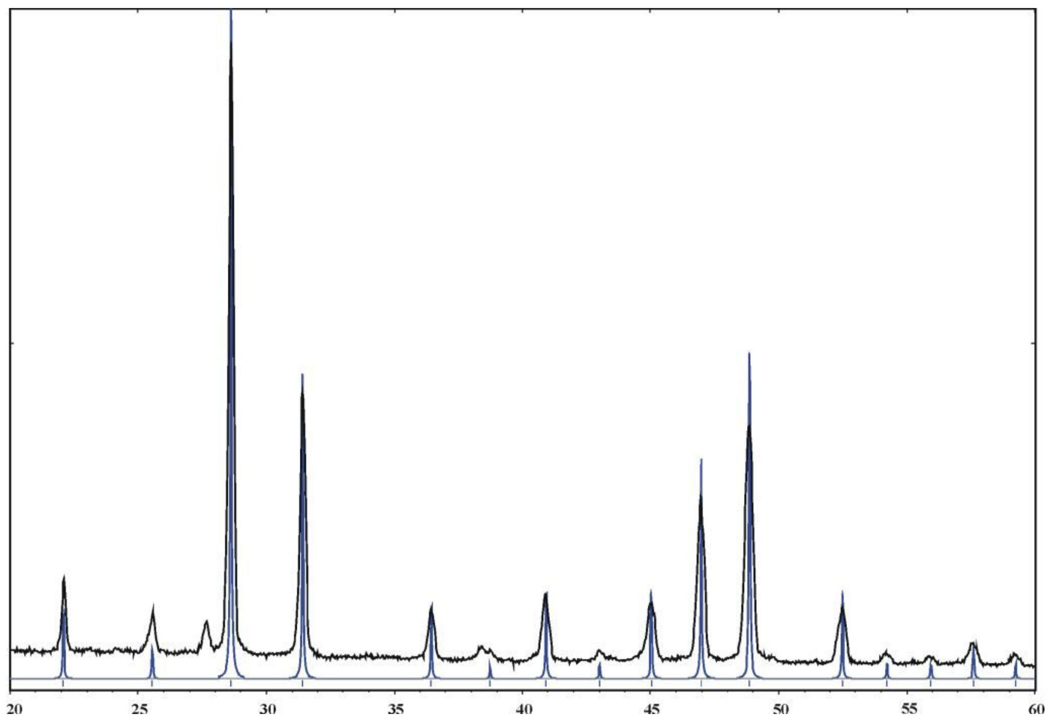

Figure 5.1. Experimental (Black) and simulated (Blue) XRD pattern of $BaCu_{5.9}SeTe_6$.

The DSC measurements were done on $BaCu_{5.9}SeTe_6$ sample, which showed its melting point as 445°C, which is almost the same melting point as that of elemental tellurium (450°C).

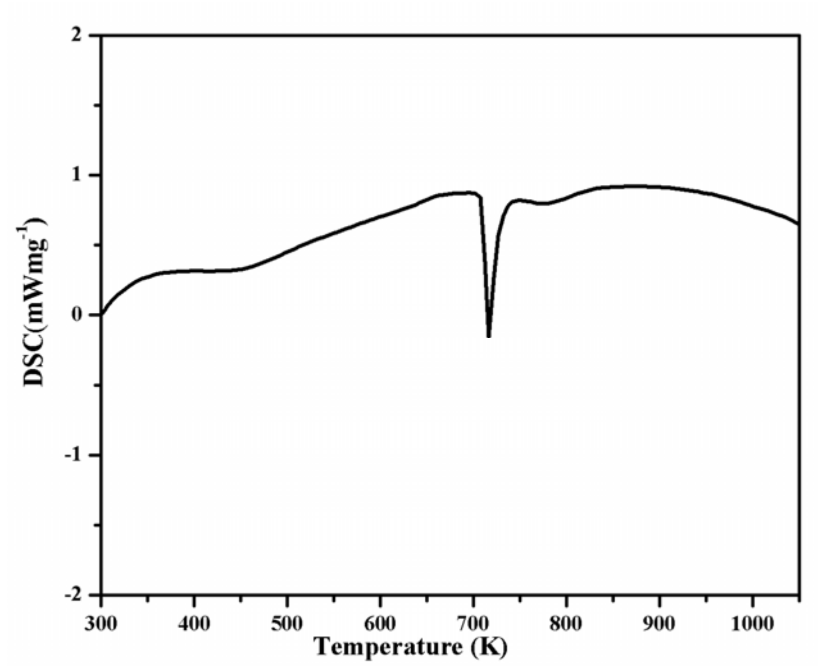

Figure 5.2 DSC curves of $BaCu_{5.9}$ $SeTe_6$.

5.2 Structure determination

Two new quaternary chalcogenides synthesized, $BaCu_{5.926(15)}SeTe_6$ (nominal composition "$Ba_4Cu_{7.6}Se_3Te_{10}$") and $BaCu_{5.72(16)}Se_{0.464(15)}Te_{6.536(15)}$ ("$Ba_4Cu_{7.6}SeTe_{12}$") are isostructural and crystallize in cubic crystal system adopting the space group $Pm\overline{3}$. The structural refinement parameters are summarized below in Table 5.1. The refinement using SHELXS yielded, one Ba, one Cu, one Te and one Se/Te mixed sites (Table 5.2 and 5.3). The occupancy of Cu1 site was refined to be only 74.1% and 71.5% for $BaCu_{5.9}SeTe_6$ and $BaCu_{5.6}Se_{0.46}Te_{6.54}$ respectively. The ADDSYMM package of PLATON was used to identify any missed symmetry elements and none was identified.

Table 5.1 Refinement details of $BaCu_{5.926(15)}SeTe_6$ and $BaCu_{5.926(15)}Se_{0.464(15)}Te_{6.536(15)}$.

Refined formula	$BaCu_{5.926(15)}SeTe_6$	$BaCu_{5.72(16)}Se_{0.464(15)}Te_{6.536(15)}$
formula weight [g/mol]	1356.79	1372.40
T of measurement [K]	296(2)	296(2)

λ [Å]	0.71073	0.71073
space group	$Pm\bar{3}$	$Pm\bar{3}$
a [Å]	6.9680(2)	6.9888(4)
V [Å^3]	338.317(17)	341.36(3)
Z	1	1
μ [mm^{-1}]	27.28	26.49
ρ_{calcd} [g/cm^3]	6.659	6.676
$R(F_o)^a$ \ $R_w(F_o^2)^b$	0.0108 \ 0.0234	0.0116 \ 0.0322

Table 5.2 Atomic coordinates, equivalent isotropic displacement parameters and occupancy factors of $BaCu_{5.927(15)}SeTe_6$.

Atom	site	x	y	z	U_{eq}/Å^2	occ.
Ba1	1*b*	0.5000	0.5000	0.5000	0.01949(14)	1
Cu1	8*i*	0.19935(5)	0.19935(5)	0.19935(5)	0.0235(2)	0.7407(19)
Te1	6*f*	0.30033(3)	0.0000	0.5000	0.01593(10)	1
Se2	1*a*	0.0000	0.0000	0.0000	0.0241(2)	1

Table 5.3 Atomic coordinates, equivalent isotropic displacement parameters and occupancy factors of $BaCu_{5.72(16)}Se_{0.464(15)}Te_{6.536(15)}$.

Atom	site	x	y	z	U_{eq}/Å^2	occ.
Ba1	1*b*	0.5000	0.5000	0.5000	0.02131(17)	1
Cu1	8*i*	0.20014(6)	0.20014(6)	0.20014(6)	0.0266(3)	0.715(2)
Te1	6*f*	0.30043(4)	0.0000	0.5000	0.01760(13)	1
Q 2	1*a*	0.0000	0.0000	0.0000	0.0562(5)	0.464(15)Se 0.536Te

5.3 Results and Discussion

5.3.1 Crystal Structures. Their structures comprise Cu–Te frameworks forming Cu_8Te_{12} pentagonal dodecahedral cage clusters similar to that of $Ti_8C_{12}^+$ [72]cluster. Many compounds with similar chalcogen frame works are known to exist, for example Cu_8S_{12} in $A_4Cu_8Ge_3S_{12}$ (A= K, Rb)[73]. Ba is encapsulated in this Cu_8Te_{12} [74]pentagonal dodecahedral cage cluster, which is formed by fusing twelve planar Cu_2Te_3 pentagons (figure 5.3a).

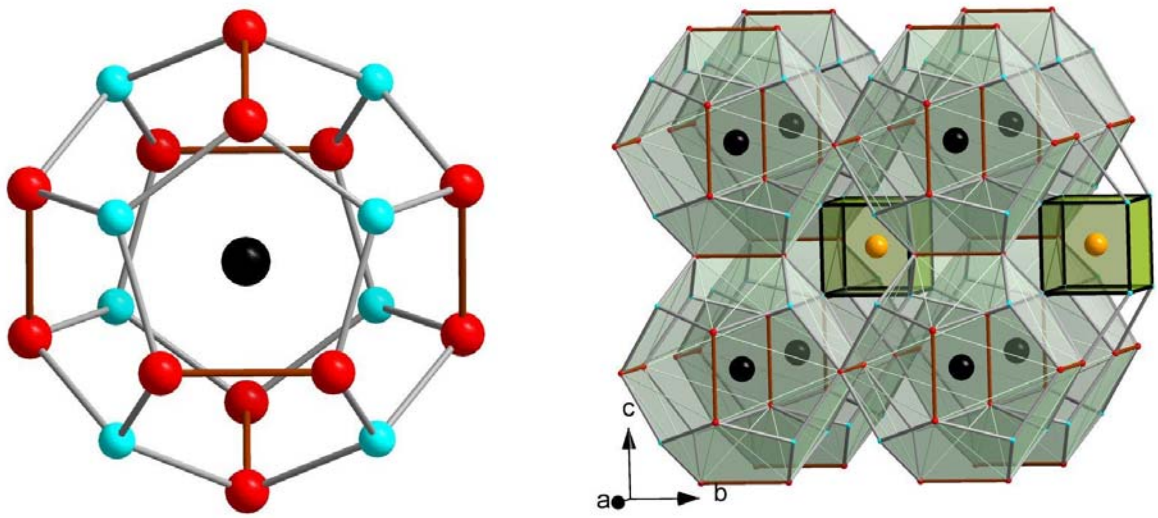

Figure 5.3 (a) Structure of $BaCu_8Te_{12}$ cage cluster (b) 3D extension of Cu_8Te_{12} cage connected by Cu_8 cube.

Another feature of this cage cluster is the presence of three mutually perpendicular sets of ditelluride units (shown by the red contacts in Figure 5.3a). These cages are extending three dimensionally in this cubic system by sharing their three ditelluride edges, as illustrated in Figure 5.3b. One copper from each cage cluster, of eight such cages, forms one Cu_8 cube containing Se atom in it. Each pentagonal face is formed by Cu_2Te_3 units with Cu–Te, Te–Te bond distances of 2.610/2.615Å and 2.783/2.7895Å respectively for $BaCu_{5.9}SeTe_6$/ $BaCu_{5.64}Se_{0.47}Te_{6.53}$. Cu forms distorted tetrahedral coordination with three Te atoms and one mixed Se/Te site wherein, the Cu–Te and Cu–Se distances of 2.610Å and 2.406Å (in $BaCu_{5.9}SeTe_6$) are observed. Angles of this distorted tetrahedron are found to be 108.16º for

Se2–Cu1–Te1 and 110.75º for Se2–Cu1–Te1. Cu1–Cu1 distance in Cu_8 cube is 2.778/2.7975 Å in $BaCu_{5.9}SeTe_6$/ $BaCu_{5.64}Se_{0.47}Te_{6.53}$ (Table 5.4).

The unit cell of $BaCu_{5.9}SeTe_6$ is shown in figure 5.4. The cation selectivity of such Cu_8Te_{12} cage was explored by Kanatzidis' group, by employing mixed alkali-alkaline earth fluxes. For example, in mixed cation compounds such as $K_2BaCu_8Te_{10}$ and $Rb_2BaCu_8Te_{10}$, Ba occupies the cage preferentially, rather than Rb or K, which in turn hints that the cage has higher affinity for cations with high charge/radius ratio (the radius should not be too small).[71]

Table 5.4 Selected interatomic distances [Å] of $BaCu_{8-x}Q_7$.

Interaction	*d*/Å [$BaCu_{5.64}Se_{0.47}Te_{6.53}$]	*d*/Å [$BaCu_{5.9}SeTe_6$]
Ba1–Te1× 12	3.7625(2)	3.7515(1)
Cu1–Te1× 3	2.6152(1)	2.6102(1)
Cu1–Te2/Se	2.4227(1)	2.406(1)
Cu1–Cu1× 3	2.7975(2)	2.7782(1)
Te1–Te1	2.7895(2)	2.7826(1)

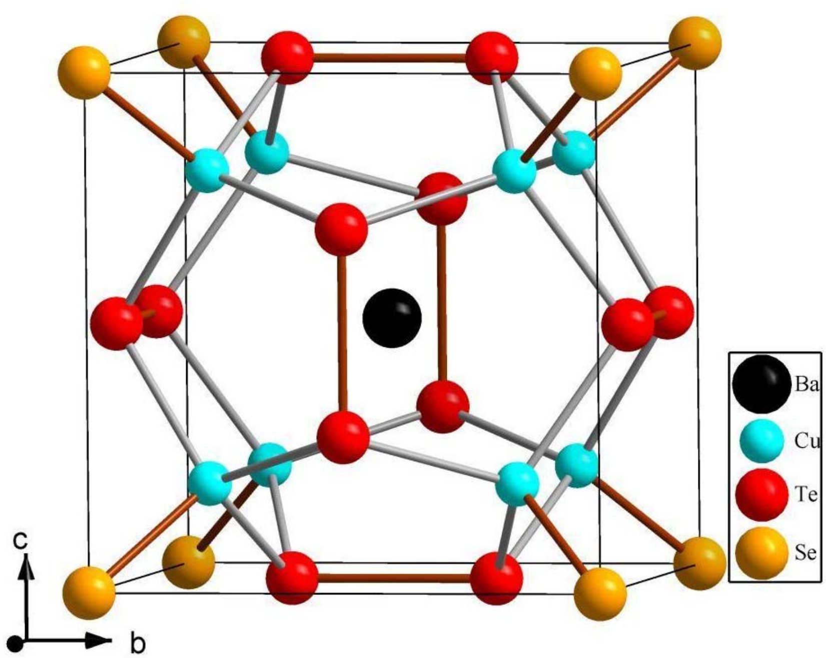

Figure 5.4 Crystal structure of $BaCu_{8-x}SeTe_6$.

5.3 Electronic structure

The electronic structure calculations were carried out using the LMTO method for these compounds. To better model the refined formula $BaCu_{5.9}SeTe_6$, we chose to remove two of the eight Cu atoms per unit cell, resulting in the formula $BaCu_6SeTe_6$, space group $R\bar{3}$ in case 1 and *Pm* in case 2. For calculations, 294 and 1008*k* for case 1 and 2, respectively, points of the irreducible wedge of the first Brillouin zone were chosen. The total DOS of the two models are shown below in the figure 5.5. The Cu-d states dominate the valence band. In both cases, a small gap appears to be present at the Fermi level.

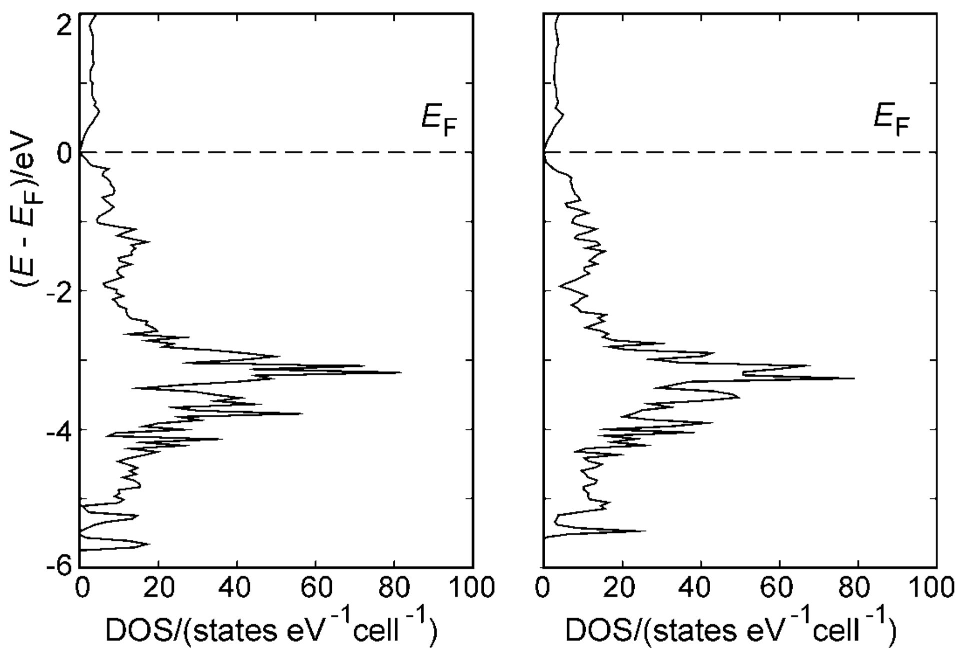

Figure 5.5 DOS of the $BaCu_6SeTe_6$ models: a) model 1 in $R\bar{3}$ space group, b) model 2 in monoclinic *Pm*.

5.4 Physical properties

The physical property measurements, i. e. evaluation of Seebeck coefficient and electrical resistivity, were performed on 13x2x2mm^3 cold-pressed pellets made from the nominal composition "$BaCu_{5.9}SeTe_6$". The measurements were done simultaneously by using ULVAC-RIKO ZEM-3 measurement system as explained in chapter 2. $BaCu_{5.9}SeTe_6$ was experimentally determined to be *p*-type doped semiconductor with moderate Seebeck coefficient value, S is 100μVK^{-1} at 300 K. The electrical resistivity, ρ, decreases with increasing temperature for $BaCu_{5.9}SeTe_6$ as shown in figure 5.6. Although assigning the formal charges on the elements as well as the electronic structure calculated for $BaCu_8SeTe_6$ pointed towards metallic nature, the presence of holes to compensate the excessive negative charge, (Ba^{2+}) $(Cu^{+1})_{5.9}$ (Se^{2-}) $(Te_2{}^{2-})_3$ could be the reason for its p-type semiconducting behavior.

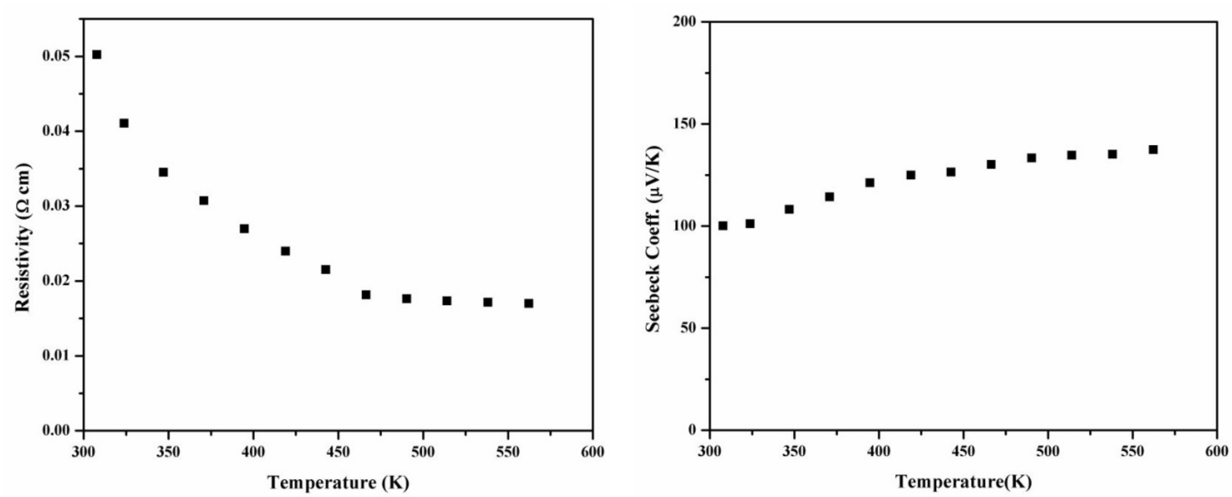

Figure 5.6 Electrical resistivity (left) and Seebeck coefficient (right) of $BaCu_{5.6}Se_{0.6}Te_{6.4}$.

Thermal conductivity of such cage compounds are known to be lower which would enhance their thermoelectric properties. For example, clathrates have large cages which contain rattling atoms inside which help reduce the lattice thermal conductivity.[3] The Ba atom inside the Cu_8Te_{12} cage may not undergo rattling since it seems to fit well in the cage and no high thermal displacement parameters are observed in our single crystal refinement studies. But in case of $Ca_{3.25}Au_{12.5}Ge_{6.5}$, Calcium atom inside similar Au_8Ge_{12} cage has high thermal displacement parameters which could be due to their rattling.[75] Thermal conductivity of $Cs_2BaCu_8Te_{10}$ and $Rb_2BaCu_8Te_{10}$ with similar Cu_8Te_{12} cages are found to be as low as ~1.4 $Wm^{-1}K^{-1}$, which is lower than that of Bi_2Te_3, a well known good thermoelectric material [1,33]. Such complex compounds with low symmetry and Cu disorder are known to possess low lattice thermal conductivity as reported in $Ba_3Cu_{14-x}Te_{12}$.[34] However, we have not measured the thermal conductivity of the newly prepared samples so far, and will be done in the future.

5.5 Conclusions

Two new compounds $BaCu_{5.9}SeTe_6$ and $BaCu_{5.64}Se_{0.47}Te_{6.53}$ belonging to a new structure type (cubic, $Pm\bar{3}$) were uncovered. They have a structurally interesting Cu_8Te_{12} cage cluster with Ba inside the cluster. However, attempts to synthesize similar compounds with varying y in $BaCu_{8-x}Se_yTe_{7-y}$ were unsuccessful. The electronic structure of the nominal composition $BaCu_8SeTe_6$ was also studied by using LMTO method, which predicted metallic character of the material. However, LMTO calculations on the Cu deficient model, $BaCu_6SeTe_6$ predicted semiconducting behavior which is proven by experimental electronic properties of these samples in the measured temperature range.

Chapter 6 Conclusion

During the present study, the following new compounds were synthesized.

1. $Ba_2Cu_{4-x}Te_5$ and $Ba_2Cu_{4-x}Se_yTe_{5-y}$
2. $Ba_2Cu_{6-x}Se_yTe_{5-y}$ and $Ba_2Cu_{6-x}S_yTe_{5-y}$
3. $BaCu_{5.93}SeTe_6$ and $BaCu_{5.72}Se_{0.46}Te_{6.54}$

The structure and bonding in these materials were studied by using single crystal X-ray diffraction method together with electronic structure calculation by using tight-binding linear muffin-tin orbital method. The band structures were calculated in order to predict or confirm the physical properties. Electronic transport properties were measured and structure-bonding-property relations in these new materials were identified.

The fractional Te–Te bonds are observed with the first series of compounds (a total of six crystals studied). The ternary telluride $Ba_2Cu_{4-x}Te_5$ crystallizes in space group $C2/c$, whereas, introduction of Se resulted in another structure type with space group $P4_12_12$. These compounds were found to be p-type semiconducting, with fairly high values of Seebeck coefficients and low conductivity. These measured parameters suggest their low efficiency as thermoelectric materials.

The second series of compounds consist of entirely different structure motifs. Here, the Cu_6 units extend along c-axis, and two such units are interconnected by S or Se atoms along a-axis. These compounds crystallize in orthorhombic system with space group *Pbam*. These compounds are nonmetallic with low Seebeck coefficients. The electronic structure calculated show semimetallic nature for the sulfide and a very narrow band gap exist for selenide compound. They have fairly large electrical conductivity, but very low values of Seebeck coefficient, which make them unsuitable for thermoelectric applications. The Power Factors calculated were very low, ranging from 2.6×10^{-7} to 6.3×10^{-6} for the sulfide and 7.8×10^{-6} to

1.2×10^{-5} for selenide within the temperatures of 350°K to550°K. Substitution with Se between $0 < y < 1$ in $Ba_2Cu_{6-x}Se_yTe_{5-y}$ is currently underway.

The third series of compounds belong to the cubic crystal system, with space group $Pm\bar{3}$. They contain Cu_8Te_{12} cages, with significant Cu-deficiency, and Ba occupies the void. One Cu atom from each cage cluster of eight such cages forms a Cu_8 cube with Se atom occupying it. Another interesting structural feature is the presence of ditelluride units. Such cage compounds are important in thermoelectric materials. The Power Factor value calculated for $BaCu_{5.6}Se_{0.6}Te_{6.4}$ is significantly higher than the other two compounds ranging from 3.3×10^{-5} to 1.0×10^{-4} between 350°K and 550°K. The substitution of Ba by various other heavy metal ions may offer improved properties and will be investigated in future.

Comparing the conductivity data of several Barium copper chalcogenides, it can be seen that the barium rich ones have high resistivity, and furthermore, the copper content increases, resistivity values decrease. This is a general conclusion where the crystal structures are not taken into account. Moreover compounds with three-dimensional network of Cu atoms show high conductivity, but such compounds are not good for thermoelectrics since they will deteriorate within days because of their copper ion mobility.

However, the copper ion mobility in the present compounds was not measured which can also be done in future. The substitution with Se was attempted in compounds such as $Ba_3Cu_{13.5}Te_{12}$ and $Ba_{6.76}Cu_{2.42}Te_{14}$, which were discovered in our group. Attempts to investigate the possibility of fractional bonding between chalcogen atoms, *Q*, were also done by attempting to prepare hypothetical compounds like "$BaCu_2Q_{2.7}$", "$Ba_2CuQ_{3.3}$", and "$BaCuQ_2$" with intermediate oxidation states of the Q atoms. These projects may be continued as future works.

Appendix A

Table A.1 Selected interatomic distances [Å] of $Ba_2Cu_{4-x}Te_5$.

Interaction	*d*/Å [$Ba_2Cu_{3.33}Te_5$]	*d*/Å [$Ba_2Cu_{3.25}Te_5$]	*d*/Å [$Ba_2Cu_{3.24}Te_5$]
Ba–Te1A/B	3.669(1) / 3.511(3)	3.6705(2) / 3.512(3)	3.674(1) / 3.524(3)
Ba–Te1A/B	3.742(2) / 4.017(3)	3.734(2) / 4.007(3)	3.741(2) / 4.003(4)
Ba–Te1A/B	3.863(3) / 3.936(4)	3.849(2) / 3.922(3)	3.845(2) / 3.923(3)
Ba–Te2A/B	3.460(3) / 3.451(6)	3.458(2) / 3.445(5)	3.463(2) / 3.454(6)
Ba–Te2A/B	3.569(3) / 3.455(6)	3.565(3) / 3.459(5)	3.563(3) / 3.458(6)
Ba–Te2A/B	3.690(3) / 3.888(5)	3.686(3) / 3.885(5)	3.699(2) / 3.888(5)
Ba–Te2A/B	3.703(2) / 3.755(5)	3.694(2) / 3.737(5)	3.695(4) / 3.746(6)
Ba–Te3	3.5040(6)	3.4942(5)	3.4971(5)
Ba–Te3	3.5425(6)	3.5330(5)	3.5339(5)
Cu1–Te1A/B	2.627(2) / 2.555(3)	2.620(2) / 2.550(3)	2.621(2) / 2.551(3)
Cu1–Te1A/B	2.682(2) / 2.345(3)	2.675(2) / 2.342(3)	2.680(2) / 2.359(4)
Cu1–Te2A/B	2.665(4) / 2.414(5)	2.655(4) / 2.405(5)	2.651(5) / 2.414(6)
Cu1–Te3	2.630(1)	2.624(1)	2.623(1)
Cu1–Cu1	2.632(2)	2.634(2)	2.642(2)
Cu1–Cu2	2.734(1)	2.717(1)	2.712(1)
Cu2–Te1A/B	2.597(1) / 2.651(3)	2.593(1) / 2.647(3)	2.598(1) / 2.641(3)
Cu2–Te1A/B	2.738(2) / 2.591(3)	2.732(1) / 2.586(3)	2.732(2) / 2.583(3)
Cu2–Te2A/B	2.669(3) / 2.552(5)	2.659(3) / 2.553(5)	2.660(3) / 2.553(6)
Cu2–Te3	2.6382(9)	2.6308(8)	2.6317(9)
Cu2–Cu1	2.734(1)	2.717(1)	2.712(1)
Cu2–Cu2	2.713(2)	2.715(2)	2.717(2)
Te1A–Te2A/B	3.028(5) / 3.316(5)	3.027(5) / 3.248(5)	3.038(6) / 3.307(7)
Te1A–Te2A/B	3.636(4) / 3.349(5)	3.618(4) / 3.309(5)	3.610(4) / 3.316(5)
Te1B–Te2A/B	3.264(4) / 2.974(6)	3.248(4) / 2.964(6)	3.247(5) / 2.976(8)
Te1B–Te2A/B	3.404(4) / 3.689(4)	3.399(4) / 3.679(6)	3.403(5) / 3.670(7)

Table A.2 Selected interatomic distances [Å] of $Ba_2Cu_{4-x}(Se,Te)_5$.

Interaction	*d*/Å		
	$Ba_2Cu_{3.26}Se_{0.73}Te_{4.27}$	$Ba_2Cu_{3.19}Se_{0.29}Te_{4.71}$	$Ba_2Cu_{3.23}Se_{0.13}Te_{4.87}$
Ba1–Te1A/B	3.615(2) / 3.497(5)	3.643(2) / 3.520(4)	3.649(2) / 3.532(4)
Ba1–Te1A/B	3.721(2) / 3.945(5)	3.763(2) / 3.980(5)	3.771(3) / 3.984(4)
Ba1–Te1A/B	3.747(2) / 3.834(5)	3.771(2) / 3.904(5)	3.779(3) / 3.912(4)
Ba1–Te2A/B	3.440(1) / 3.43(1)	3.468(2) / 3.433(8)	3.468(3) / 3.442(6)
Ba1–Te2A/B	3.488(2) / 3.36(2)	3.540(4) / 3.461(9)	3.560(4) / 3.461(6)
Ba1–Te2A/B	3.675(2) / 3.87(2)	3.694(4) / 3.85(1)	3.690(4) / 3.840(7)
Ba1–Te2A/B	3.691(2) / 3.82(2)	3.699(4) / 3.77(1)	3.696(4) / 3.790(7)
Ba1–*Q*3	3.4305(7)	3.4716(6)	3.4883(5)
Ba1–*Q*3	3.4735(7)	3.5112(6)	3.5223(5)
Cu1–Te1A/B	2.594(2) / 2.604(5)	2.560(2) / 2.586(4)	2.603(2) / 2.586(5)
Cu1–Te1A/B	2.685(3) / 2.404(5)	2.694(3) / 2.417(5)	2.701(3) / 2.428(5)
Cu1–Te2A/B	2.581(3) / 2.39(2)	2.634(7) / 2.43(1)	2.652(5) / 2.451(7)
Cu1–*Q*3	2.522(1)	2.596(1)	2.6168(9)
Cu1–Cu2	2.625(2)	2.670(1)	2.694(1)
Cu1–Cu2	2.769(2)	2.712(1)	2.694(1)
Cu2–Te1A/B	2.630(2) / 2.557(5)	2.625(2) / 2.558(4)	2.625(2) / 2.556(4)
Cu2–Te1A/B	2.682(3) / 2.530(5)	2.704(3) / 2.509(5)	2.713(2) / 2.519(5)
Cu2–Te2A/B	2.617(4) / 2.37(2)	2.651(5) / 2.53(1)	2.672(5) / 2.523(7)
Cu2–*Q*3	2.506(1)	2.5827(9)	2.6039(8)
Cu2–Cu1	2.625(2)	2.670(1)	2.694(1)
Cu2–Cu1	2.769(2)	2.712(1)	2.694(1)
Te1A–Te2A/B	3.021(6) / 3.18(3)	3.032(9) / 3.32(1)	3.016(7) / 3.284(8)
Te1A–Te2A/B	3.528(6) / 3.37(3)	3.580(9) / 3.28(1)	3.617(5) / 3.346(7)
Te1B–Te2A/B	3.196(7) / 2.85(3)	3.22(1) / 2.97(1)	3.262(8) / 2.990(7)
Te1B–Te2A/B	3.358(6) / 3.70(3)	3.40(1) / 3.65(1)	3.377(5) / 3.644(8)

Table A.3 Selected interatomic distances [Å] of $Ba_2Cu_{6-x}Q_5$.

Interaction	*d*/Å [$Ba_2Cu_{5.53}STe_4$]	*d*/Å [$Ba_2Cu_{5.64}Se_{1.09}Te_{3.91}$]
Ba1–S1/Se1×2	3.1420(1)	3.2270(1)
Ba1–Te1	3.5003(2)	3.5608(2)
Ba1–Te2/Se2×2	3.5579(2)	3.5622(2)
Ba1–Te2/Se2×2	3.6100(1)	3.5883(1)
Ba1–Te1	3.7699(2)	3.7448(2)
Cu1–Te1	2.6645(2)	2.6732(2)
Cu1–Te1	2.7741(2)	2.7962(2)
Cu1–Te2/Se2×2	2.7217(1)	2.7472(1)
Cu1–Cu2×2	2.5637(1)	2.5768(1)
Cu1–Cu3×2	2.8172(1)	2.7692(1)
Cu2–Te1×2	2.5984(1)	2.6236(1)
Cu2–Te2/Se2	2.5760(1)	2.5735(1)
Cu2–Cu2	2.5844(2)	2.6613(2)
Cu2–Cu3	2.9392(2)	2.8423(2)
Cu2–Cu3	2.5994(1)	2.5832(1)
Cu3–Te1×2	2.7181(1)	2.7248(1)
Cu3–Te2/Se2	2.6874(2)	2.6631(2)
Cu3–S1/Se1	2.3809(1)	2.4997(2)

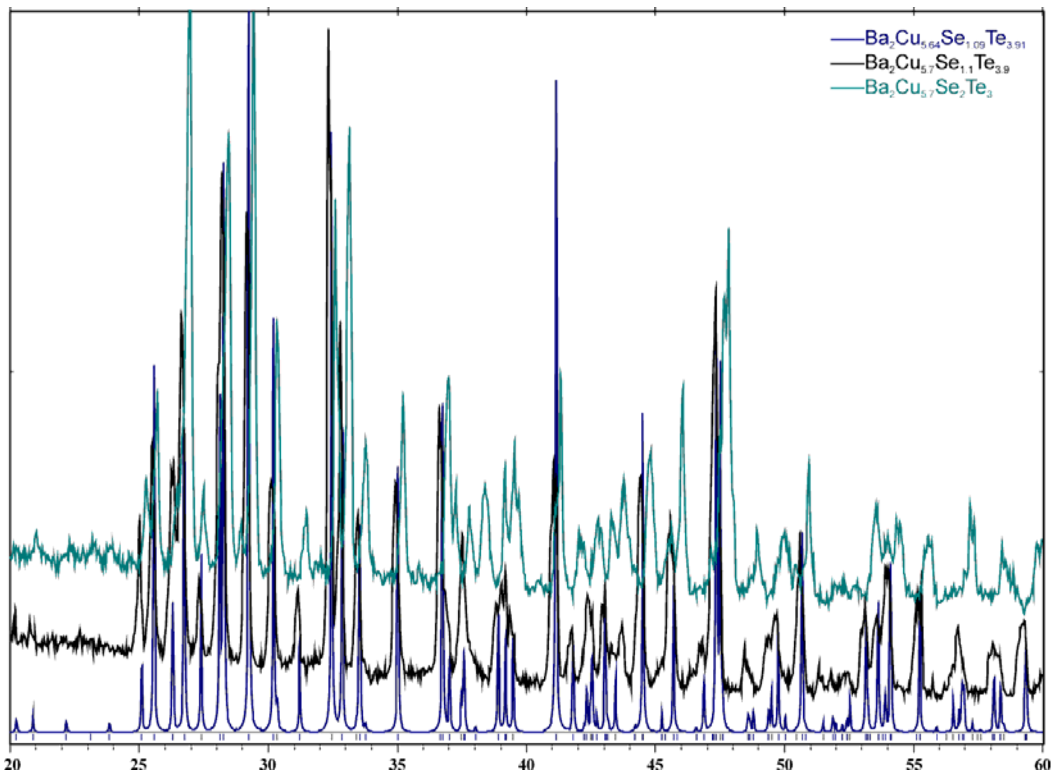

Figure A.1 Comparison of experimental and simulated XRD pattern of $Ba_2Cu_{5.64}Se_yTe_{5-y}$

Table A.4 Attempted compositions in 2-6-5 system.

$Ba_2Cu_{5.53}S_4Te$	$Ba_2Cu_6STe_4$
$Ba_2Cu_{5.53}S_5$	$Ba_2Cu_{5.7}Se_2Te_3$
$Ba_2Cu_{5.53}Te_5$	$Ba_2Cu_{5.7}Se_3Te_2$
$Ba_2Cu_{5.53}Se_4S$	$Ba_2Cu_{5.7}Se_4Te$
$Ba_2Cu_{5.53}SeTe_4$	$Ba_2Cu_{5.7}Se_5$
$Ba_2Cu_{5.7}Se_{1.1}Te_{3.9}$	$Ba_2Ag_6STe_4$
$Ba_2Au_6STe_4$	

REFERENCES

(1) Rowe, D. M. *CRC Handbook of Thermoelectrics*; CRC Press: Boca Raton, FL, **1995**.

(2) Tritt, T. M.; Subramanian, M. A. *MRS Bulletin* **2006**, *31*, 188-194.

(3) Snyder, G. J.; Toberer, E. S. *Nature Mater.* **2008**, *7*, 105-114.

(4) Caillat, T.; Fleurial, J. P.; Borshchevsky, A. *Journal of Physics and Chemistry of Solids* **1997**, *58*, 1119-1125.

(5) Brown, S. R.; Kauzlarich, S. M.; Gascoin, F.; Snyder, G. J. *Chem. Mater.* **2006**, *18*, 1873-1877.

(6) Dashjav, E.; Szczepenowska, A.; Kleinke, H. *J. Mater. Chem.* **2002**, *12*, 345-349.

(7) Xu, H.; Kleinke, K. M.; Holgate, T.; Zhang, H.; Su, Z.; Tritt, T. M.; Kleinke, H. *J. Appl. Phys.* **2009**, *105*, 053703/1-053703/5.

(8) Jensen, P.; Kjekshus, A.; Skansen, T. *Acta Chem. Scand.* **1966**, *20*, 417-422.

(9) Kleinke, H. In *Inorganic Chemistry in Focus II*; Meyer, G., Naumann, D., Wesemann, L., Eds.; Wiley-VCH: Weinheim, Germany, 2004, p 167-191.

(10) Xu, J.; Kleinke, H. *J. Comput. Chem.* **2008**, *29*, 2134-2143.

(11) *Inorganic Chemistry Highlights*; Miller, J. G.; Lee, C. S.; Choe, W., Eds.; Wiley-VCH, Germany., **2002**.

(12) Xue, Y. J.; Liu, K. G.; Lia, J. H.; Chen, N. *Materials Research Bulletin* **2005**, *40*, 1172-1176.

(13) Eisenmann, B. *Z. Naturforsch.* **1979**, *34B*, 1162-1164.

(14) Hirschle, C.; Roehr, C. *Z. Anorg. Allg. Chem.* **2000**, *626*, 1992-1998.

(15) Smith, D. M.; Ibers, J. A. *Coord. Chem. Rev.* **2000**, *200-202*, 187-205.

(16) Bottcher, P.; Doert, T. *Phosphorus Sulfur and Silicon and the Related Elements* **1998**, *136*, 255-282.

(17) Bottcher, P. *Angewandte Chemie-International Edition in English* **1988**, *27*, 759-772.

(18) Bottcher, P.; Kretschmann, U. *Zeitschrift Fur Anorganische Und Allgemeine Chemie* **1982**, *491*, 39-46.

(19) Bottcher, P.; Kretschmann, U. *Journal of the Less-Common Metals* **1983**, *95*, 81-91.

(20) Bernstein, J.; Hoffmann, R. *Inorg. Chem.* **1985**, *24*, 4100-4108.

(21) Klaiber, F.; Petter, W.; Hulliger, F. *Journal of Solid State Chemistry* **1983**, *46*, 112-120.

(22) Marsh, R. E. *Journal of Solid State Chemistry* **1990**, *87*, 467-468.

(23) Walton, P. D.; Sutherland, H. H.; Hogg, J. H. C. *Acta Crystallographica Section B-Structural Science* **1978**, *34*, 41-45.

(24) Stowe, K. *Journal of Solid State Chemistry* **2000**, *149*, 123-132.

(25) Assoud, A.; Derakhshan, S.; Soheilnia, N.; Kleinke, H. *Chem. Mater.* **2004**, *16*, 4193-4198.

(26) Ansari, M. A.; Bollinger, J. C.; Ibers, J. A. *J. Am. Chem. Soc.* **1993**, *115*, 3838-3839.

(27) Bottcher, P.; Kretschmann, U. *Zeitschrift Fur Anorganische Und Allgemeine Chemie* **1985**, *523*, 145-152.

(28) Assoud, A.; Xu, J.; Kleinke, H. *Inorg. Chem.* **2007**, *46*, 9906-9911.

(29) Tritt, T. M. *Science* **1995**, *272*, 1276-1277.

(30) DiSalvo, F. J. *Science* **1999**, *285*, 703-706.

(31) Rowe, D. M. *Thermoelectrics Handbook: Macro to Nano*; CRC Press, Taylor & Francis Group: Boca Raton, FL, USA, 2006.

(32) Wang, Y. C.; DiSalvo, F. J. *J. Solid State Chem.* **2001**, *156*, 44-50.

(33) Patschke, R.; Zhang, X.; Singh, D.; Schindler, J.; Kannewurf, C. R.; Lowhorn, N.; Tritt, T.; Nolas, G. S.; Kanatzidis, M. G. *Chem. Mater.* **2001**, *13*, 613-621.

(34) Assoud, A.; Thomas, S.; Sutherland, B.; Zhang, H.; Tritt, T. M.; Kleinke, H. *Chem. Mater.* **2006**, *18*, 3866-3872.

(35) Cui, Y.; Assoud, A.; Xu, J.; Kleinke, H. *Inorg. Chem.* **2007**, *46*, 1215-1221.

(36) Zhang, X.; Schindler, J. L.; Hogan, T.; Albritton-Thomas, J.; Kannewurf, C. R.; Kanatzidis, M. G. *Angew. Chem. Int. Ed. Engl.* **1995**, *34*, 68-71.

(37) Kuropatwa, B.; Cui, Y.; Assoud, A.; Kleinke, H. *Chem. Mater.* **2009**, *21*, 88-93.

(38) *SAINT*; Version 4 ed.; Siemens Analytical X-ray Instruments Inc.: Madison, WI., 1995.

(39) Sheldrick, G. M. *SHELXTL*; Version 5.12 ed.; Siemens Analytical X-Ray Systems: Madison, WI., 1995.

(40) Dronskowski, R.; Blöchl, P. E. *J. Phys. Chem.* **1993**, *97*, 8617-8624.

(41) Andersen, O. K. *Phys. Rev. B* **1975**, *12*, 3060-3083.

(42) Skriver, H. L. *The LMTO Method*; Springer: Berlin, Germany, 1984.

(43) Hedin, L.; Lundqvist, B. I. *J. Phys. C* **1971**, *4*, 2064-2083.

(44) Yao, X.; Marking, G.; Franzen, H. F. *Ber. Bunsenges.* **1992**, *96*, 1552-1557.

(45) Köckerling, M.; Franzen, H. F. *Croat. Chem. Acta* **1995**, *68*, 709-719.

(46) Yao, X.; Franzen, H. F. *J. Am. Chem. Soc.* **1991**, *113*, 1426-1427.

(47) Yao, X.; Miller, G. J.; Franzen, H. F. *J. Alloys Compd.* **1992**, *183*, 7-17.

(48) Yao, X.; Franzen, H. F. *J. Solid State Chem.* **1990**, *86*, 88-93.

(49) Yao, X.; Franzen, H. F. *Z. Anorg. Allg. Chem.* **1991**, *598-599*, 353-362.

(50) Kleinke, H. *J. Am. Chem. Soc.* **2000**, *122*, 853-860.

(51) Kleinke, H. *Chem. Commun.* **1998**, 2219-2220.

(52) Kleinke, H.; Franzen, H. F. *J. Am. Chem. Soc.* **1997**, *119*, 12824-12830.

(53) Warczok, P.; Chumak, I.; Richter, K. W. *J Solid State Chem.* **2009**, *182*, 896-904.

(54) Richter, K. W.; Flandorfer, H.; Franzen, H. F. *J. Solid State Chem.* **2002**, *167*, 517-524.

(55) Kleinke, H. *Trends Inorg. Chem.* **2001**, *7*, 135-149.

(56) Kleinke, H. *J. Alloys Compd.* **2002**, *336*, 132-137.

(57) Debus, S.; Harbrecht, B. *Z. Anorg. Allg. Chem.* **2001**, *627*, 431-438.

(58) Doert, T.; Fokwa, B. P. T.; Simon, P.; Lidin, S.; Söhnel, T. *Chem. Eur. J.* **2003**, *9*, 5865-5872.

(59) Böttcher, P.; Keller, R. *J. Less-Common Met.* **1985**, *109*, 311-321.

(60) Mehrotra, P. K.; Hoffmann, R. *Inorg. Chem.* **1978**, *17*, 2187-2189.

(61) Merz Jr., K. M.; Hoffmann, R. *Inorg. Chem.* **1988**, *27*, 2120-2127.

(62) Pyykkö, P. *Chem. Rev.* **1997**, *97*, 597-636.

(63) Assoud, A.; Cui, Y.; Thomas, S.; Sutherland, B.; Kleinke, H. *J. Solid State Chem.* **2008**, *181*, 2024-2030.

(64) Jepsen, O.; Andersen, O. K. *Z. Phys.* **1995**, *97*, 35-47.

(65) Landrum, G. A.; Dronskowski, R. *Angew. Chem. Int. Ed.* **2000**, *39*, 1560-1585.

(66) Assoud, A.; Soheilnia, N.; Kleinke, H. *Z. Naturforsch.* **2004**, *59b*, 975-979.

(67) Iglesias, J. E.; Pachali, K. E.; Steinfink, H. *J. Solid State Chem.* **1974**, *9*, 6-14.

(68) Assoud, A.; Derakhshan, S.; Soheilnia, N.; Kleinke, H. *Proc. Int. Conf. Thermoelec.* **2005**, *24*, 303-310.

(69) Mayasree, O.; Cui, Y.; Assoud, A.; Kleinke, H. *Inorg. Chem.* **2010**, *49*, 6518–6524.

(70) Park, Y.; Kanatzidis, M. G. *Chem. Mat.* **1991**, *3*, 781-783.

(71) Zhang, X.; Park, Y.; Hogan, T.; Schindler, J. L.; Kannewurf, C. R.; Seong, S.; Albright, T.; Kanatzidis, M. G. *J. Am. Chem. Soc.* **1995**, *117*, 10300-10.

(72) Guo, B. C.; Kerns, K. P.; Castleman, J., A. W *Science* **1992**, *255*, 1411-1413.

(73) Zhang, R.-C.; Yao, H.-G.; Ji, S.-H.; Liu, M.-C.; An, Y.-L. *Inorg. Chem.* **2010**, *49*, 6372-6374.

(74) Poblet, J. M.; Rohmer, M.-M.; Bénard, M. *Inorg. Chem.* **1996**, *35*, 4073-4075.

(75) Lin, Q.; Corbett, J. D. *Inorg. Chem.* **2010**, *49*, 4570-4577.